

Physical Models for the Astrophysical Population of Black Holes: Application to the Bump in the Mass Distribution of Gravitational Wave Sources

JACOB GOLOMB,^{1,2} MAXIMILIANO ISI,³ AND WILL M. FARR^{3,4}

¹*Department of Physics, California Institute of Technology, Pasadena, California 91125, USA*

²*LIGO Laboratory, California Institute of Technology, Pasadena, California 91125, USA*

³*Center for Computational Astrophysics, Flatiron Institute, 162 5th Ave, New York, NY 10010, USA*

⁴*Department of Physics and Astronomy, Stony Brook University, Stony Brook NY 11794, USA*

(Dated: December 8, 2023)

ABSTRACT

Gravitational wave observations of binary black holes have revealed unexpected structure in the black hole mass distribution. Previous studies of the mass distribution employ physically-motivated phenomenological models and infer the parameters that directly control the features of the mass distribution that are allowed in their model, associating the constraints on those parameters with their physical motivations. In this work, we take an alternative approach in which we introduce a model parameterizing the underlying stellar and core-collapse physics and obtaining the remnant black hole distribution as a derived byproduct. In doing so, we directly constrain the stellar physics necessary to explain the astrophysical distribution of black hole properties under a given model. We apply this approach to modeling the mapping between stellar core mass and remnant black hole mass, including the effects of mass loss due to the pulsational pair instability supernova (PPISN) process, which has been proposed as an explanation for the observed excess of black holes at $\sim 35M_{\odot}$. Placing constraints on the nuclear reaction rates necessary to explain the PPISN parameters, we conclude that the peak observed at $\sim 35M_{\odot}$ is highly unlikely to be a signature from the PPISN process. This procedure can be applied to modeling any physical process that underlies the astrophysical mass distribution. Allowing the parameters of the core-remnant mass relationship to evolve with redshift permits correlated and physically reasonable changes in the location, shape, and amplitude of features in the mass function. We find that the current data are consistent with no redshift evolution in the core-remnant mass relationship, but ultimately place only weak constraints on the change of these parameters.

1. INTRODUCTION

Observations of gravitational waves from binary-black-hole (BBH) and binary-neutron-star (BNS) mergers with the LIGO-Virgo-KAGRA detector network have provided otherwise inaccessible information on the properties of those compact objects (Abbott et al. 2018; Aasi et al. 2015; Acernese et al. 2015). While individual events offer a glimpse into the details of a particular black hole or neutron star, studying observations collectively on a population-level allows us to draw inferences about stellar astrophysics, the formation channels of black holes and neutron stars, the overall rates at which BBH/BNS mergers occur in the universe, and cosmology (LIGO Scientific Collaboration et al. 2023a,b,c;

LIGO Scientific Collaboration & Virgo Collaboration 2021), as well as tests of general relativity (Abbott et al. 2021; Payne et al. 2023).

Models adopted for population inference of BBHs tend to take one of two major approaches. The first are so-called parametric methods, in which a phenomenological model is constructed using relatively few parameters, with these parameters directly controlling well-defined features encoded in the model. This commonly involves assuming a functional form for the global structure of the distribution (e.g., a truncated power law for the mass distribution), enhanced by features such as a bump, dip, or break, and jointly fitting for the properties of the global structure and additional features (Talbot & Thrane 2018; LIGO Scientific Collaboration & Virgo Collaboration 2021; LIGO Scientific Collaboration et al. 2023a; Kovetz et al. 2017; Fishbach & Holz 2017). The

other popular approach consists of data-driven methods (sometimes called “non-parametric” methods, in spite of their overabundance of parameters) in which a flexible model is allowed to fit nearly-arbitrary shapes to the distribution. Such fits have been achieved with tools such as splines, histograms, and Gaussian process regression (Callister & Farr 2023; Golomb & Talbot 2023; Mandel et al. 2017; Ray et al. 2023; Edelman et al. 2022; Tiwari & Fairhurst 2021). While the latter method is more general and can capture features not explicitly defined in a model, the former offers the ability to encode signatures from expected physical processes in parameters controlling the shape of the distribution, making it possible to interpret the constraints in terms of the underlying physical motivations. However, interpreting the constraints on these parameters as constraints on the underlying physics can be difficult, as there are often unmodeled assumptions as to how the underlying physical processes translate into resulting distribution that is being modeled.

In this work, we provide an alternative approach to prescribing a parametric population model: instead of modeling the BBH distribution directly, we introduce parameters to describe the underlying astrophysics and the associated mapping to remnant black hole properties and we derive the resulting population distribution as a result of these underlying parameters and its associated mapping. Subject to model assumptions, we more directly infer the physics as informed by BBH properties in a way that avoids strong phenomenological approximations in the BBH population model itself. This is related to the “backpropagation” approach in Wong et al. (2023) and the related method in Andrews et al. (2021).

Previous parametric approaches to modeling the BBH mass distribution have been particularly useful to place constraints with relatively little data when strong assumptions about the structure of the mass distribution are warranted. For example, parametric population analyses of the first catalogs of BBH events have revealed that the mass distribution is well-described by a truncated power law that peaks at $\sim 8 M_{\odot}$, decaying to high masses, and featuring an overdensity (modeled as a Gaussian bump) at $\sim 35 M_{\odot}$ (LIGO Scientific Collaboration et al. 2023a; LIGO Scientific Collaboration & Virgo Collaboration 2021).

We apply our novel approach to explain this overdensity in the mass distribution at $\sim 35 M_{\odot}$, which may or may not be accompanied by a subsequent dip (Talbot & Thrane 2018; Edelman et al. 2022). The original motivation for allowing for this feature in the mass distribution was to capture the expected “pile-up” of black

holes that resulted from progenitors that had undergone pair instability pulsations (Talbot & Thrane 2018). This pile-up results from the remnants of stars with zero-age main-sequence (ZAMS) masses between $\sim 60 M_{\odot}$ through $\sim 140 M_{\odot}$ (Rahman et al. 2022; Woosley & Heger 2021; Woosley 2017). As stars in this mass range evolve past the helium burning phase, their cores reach temperatures hot enough to produce electron-positron pairs, reducing radiation pressure and softening the star’s equation of state, which causes the star to contract (Fowler & Hoyle 1964; Rakavy & Shaviv 1967). This contraction can explosively ignite oxygen in the core, driving an outward pulse that removes varying amounts of mass from the star. The star then returns to a contracting phase and the cycle can repeat itself until enough mass has been shed that it evolves toward normal core collapse. For stars with ZAMS masses above this range, the contraction-driven core ignition drives a shock that completely disrupts the star, leaving behind no remnant. Since the pulsational pair instability process produces a small range of remnant black hole masses from stars from a wide range of ZAMS masses, it is expected that the mass distribution will exhibit the bump due to this pileup (sometimes referred to as the “pulsational-pair-instability supernova (PPISN) graveyard”) followed by a suppression of sources, known as the upper mass gap (Woosley 2017, 2019; Woosley & Heger 2021; Farmer et al. 2019).

Simulations of stellar evolution (e.g. Farmer et al. (2019); Mehta et al. (2022); Farag et al. (2022)) have explored the relationship between initial stellar mass (in particular the mass of the Carbon-Oxygen (CO) core, M_{CO}) and the final black hole mass (M_{BH}) after core collapse. They have also quantified the dependence of the location of the lower edge of the upper mass gap and its associated mass range on other physical parameters such as reaction rates, metallicity, and details of assumed neutrino physics. Previous studies have used this relationship to place constraints on the astrophysical properties of the pulsational pair instability process, assuming the most massive sources observed through LIGO are below the upper mass gap (Farmer et al. 2020; Mehta et al. 2022; Farag et al. 2022; Stevenson et al. 2019). Baxter et al. (2021) instead infers the population of black holes coming from the first-generation (1G) subpopulation below the upper mass gap along with the subpopulation of higher-generation (2G+) black holes whose masses can lie within the upper mass gap.

In this work, we implement a simple model for the initial mass function of stellar CO cores and the associated map from CO core mass to remnant mass, motivated by the relationship found from the simulations

in Farmer et al. (2019, 2020). Rather than informing our model with individual massive sources, we construct a full population model for the mass distribution, including a subpopulation in the upper mass gap due to higher-generation mergers. Using data from gravitational wave events from the third Gravitational Wave Transient Catalog (GWTC-3, LIGO Scientific Collaboration et al. (2023c)), we infer the shape of the initial mass function of CO cores, the associated mapping to the remnant BH distribution, and the relative contribution of sources formed through 1G mergers.

Having a physically-motivated model for the black hole mass distribution facilitates extensions that incorporate richer physics. As an example, here we allow the underlying physics to evolve with redshift, as may be expected from cosmic history considerations. Such evolution in the underlying physical parameters captures the correlated changes in shape and height of the bump that must occur in the presence of changing progenitor to remnant mass relationships. It may be possible to use shape measurements to calibrate changes in the mass scale of the bump with redshift to reduce or eliminate systematic uncertainties in cosmological parameter inference from the BBH mass function, sometimes called the “spectral siren” method (Farr et al. 2019; Ezquiaga & Holz 2022).

While this approach is applied to modeling the PPISN process underlying the astrophysical BBH mass distribution, it can more generally be used as a model to place constraints on any relationship between progenitor mass and remnant black hole mass as informed by gravitational wave observations. The model introduced here can readily be applied to any process with accelerating mass loss as a function of progenitor mass, but this method can be useful for inferring the physics of any arbitrary relationship underlying an observable distribution associated with BBHs (c.f. Fishbach & van Son (2023) for a related approach applied to inferring the delay times between binary formation and merger).

We begin with an overview of hierarchical Bayesian inference in Sec. 2. We then outline the models with and without evolution with redshift in Sec. 3. In Sec. 4, we present results for both model configurations, using data from the third observing run (O3) of LIGO-Virgo. We offer interpretations of our results in Sec. 5 and provide concluding remarks in Sec. 6.

2. HIERARCHICAL BAYESIAN INFERENCE

We conduct our inference on the population parameters Λ with a hierarchical Bayesian framework, in which we inform our population model with a catalog N_{det}

events, to compute the likelihood (see, e.g., Mandel et al. (2019); Thrane & Talbot (2019)):

$$\mathcal{L}(\{d\}|\Lambda) \propto \frac{K(\Lambda)^{N_d} e^{-K(\Lambda)}}{p_{\text{det}}(\Lambda)^{N_d}} \prod_{i=1}^{N_{\text{det}}} \int \mathcal{L}(d_i|\theta) \pi(\theta|\Lambda) d\theta \quad (1)$$

where $\mathcal{L}(d_i|\theta)$ is the likelihood of the data for the i th event, given physical parameters θ (i.e., masses, distances), and $\pi(\theta|\Lambda)$ is our population model with a predicted number of detections K . The $p_{\text{det}}(\Lambda)$ prefactor accounts for the selection effects associated with observing a catalog biased toward sources with parameters that favor detectability (i.e., the Malmquist bias). See Appendix A for details on this likelihood.

Following the approach in Farr (2019) and Tiwari (2018), we compute $p_{\text{det}}(\Lambda)$ with injections of sources from a fiducial population in detector noise, and assigning weights to each of the sources that pass our detection threshold. These sensitivity injections are from the O3 injection set released in LIGO Scientific Collaboration et al. (2023d). We compute the per-event population evidence (the integral in Eq. (1)) by reweighting samples from individual event posterior distributions and dividing by the event-specific sampling priors. Since our population model is written only in terms of masses and distances, we effectively adopt the prior from parameter estimation for the spin parameters (isotropic in direction and uniform in spin magnitude).

For our analyses involving third observing run (O3) data, we obtain posterior samples for each event from LIGO Scientific Collaboration et al. (2021), using the same BBH events from O3 as in LIGO Scientific Collaboration et al. (2023a). This results in 59 events meeting the False Alarm Rate (FAR) threshold of 1 per year. Throughout this work we assume the best-fit cosmological parameters from the Planck 2018 release (Planck Collaboration 2020).

We sample the population posterior using the No-U-Turn-Sampler (NUTS) in `Numpyro` (Phan et al. 2019; Bingham et al. 2019), and we write the functions for computing Eq. (1) in `jax` (Bradbury et al. 2018) to take advantage of automatic differentiation when sampling with Hamiltonian Monte Carlo (Duane et al. 1987).

3. MASS DISTRIBUTION OF BLACK HOLES FROM CO CORE IMF

3.1. Mass Distribution Model

We begin to construct our mass distribution model by assuming a functional form for the initial mass function (IMF) of stellar CO cores. Surveys have shown that the stellar IMF on the main sequence can be well-modeled

as a featureless power law at high masses, with a power law index of ~ -2.3 (see, e.g., Kroupa 2001; Salpeter 1955; Kroupa & Jerabkova 2019). Recent studies have shown through simulations and analytic approximations that there may be an approximately linear relationship between a high-mass star’s zero-age main-sequence (ZAMS) mass and the mass of its core before undergoing supernova, although this is uncertain (Woosley 2019; Belczynski et al. 2016). We therefore assume that the IMF of CO cores can also be modeled with a power law to good approximation, but allow for a break at $20 M_{\odot}$ for additional flexibility (see, e.g., Schneider et al. 2018). Even if this relationship has nontrivial nonlinearities, modelling the shape of the broken power law should capture the dominant resolvable structure of the distribution.

We express the distribution CO core masses, M_{CO} , as

$$\frac{dN}{dM_{\text{CO}}}(M_{\text{CO}}) \propto \begin{cases} \left(\frac{M_{\text{CO}}}{20M_{\odot}}\right)^{-a} & \text{if } M_{\text{CO}} < 20M_{\odot}, \\ \left(\frac{M_{\text{CO}}}{20M_{\odot}}\right)^{-b} & \text{if } M_{\text{CO}} > 20M_{\odot}. \end{cases} \quad (2)$$

In order to obtain the resulting BH mass distribution from the CO core mass distribution, we require a map-

$$\bar{M}_{\text{BH}}(M_{\text{CO}}|M_{\text{PISN}}, M_{\text{BHmax}}) = \begin{cases} M_{\text{CO}} & \text{if } M_{\text{CO}} < M_{\text{PPISN}}, \\ M_{\text{BHmax}} + \frac{(M_{\text{CO}} - 2M_{\text{BHmax}} + M_{\text{PPISN}})^2}{4(M_{\text{PPISN}} - M_{\text{BHmax}})} & \text{if } M_{\text{PPISN}} < M_{\text{CO}} < 2M_{\text{BHmax}} - M_{\text{PPISN}}, \\ 0 & \text{otherwise.} \end{cases} \quad (3)$$

This captures the linear relationship at lower masses, for which the relative amount of mass loss in core collapse is independent of M_{CO} ; it then transitions to a quadratic function at the onset of pulsations, M_{PPISN} , with the range M_{PPISN} to $M_{\text{BH,max}}$ approximately representing the range of final BH masses that “pile up” to form a feature in the BH mass distribution. This pile-up is usually expressed as a relative overdensity through a Gaussian bump (Talbot & Thrane 2018; LIGO Scientific Collaboration & Virgo Collaboration 2021; LIGO Scientific Collaboration et al. 2023a).

When M_{CO} reaches M_{PPISN} , the M_{CO} to M_{BH} mapping transitions from its linear relationship to a nonlinear one as the pulsation process causes mass loss whose efficiency increases with the star’s mass (Marchant et al. 2019; Farmer et al. 2019; Woosley 2017; Woosley & Heger 2021). The form of the quadratic function in Eq. (3) puts the peak value at $M_{\text{BH,max}}$ and enforces that the transition and its derivative be continuous at M_{PPISN} . This results in a BH mass distribution in which

ping between M_{CO} for a star and the mass of its remnant after undergoing core collapse. From simulations with the stellar evolution code MESA (Paxton et al. 2019), Farmer et al. (2019) find that M_{CO} prior to core collapse is in fact the dominant variable determining the remnant mass post core collapse. Figure 4 in Farmer et al. (2019) shows the resulting M_{BH} vs M_{CO} relationships obtained for a range of choices of input physics and metallicity. The authors note that for a given choice of metallicity, this relationship is well-modeled by a piecewise map: a linear relationship, turning over to a quadratic at the CO core mass at which pulsations begin to remove notable mass, followed by a decay to $M_{\text{BH}} = 0 M_{\odot}$, corresponding to the mass at which pulsational pair instability fully disrupts the star, leaving no remnant. This general trend has been confirmed by other simulation-based studies (e.g., Mehta et al. 2022; Woosley 2017).

We express this piecewise mapping through a functional form $\bar{M}_{\text{BH}}(M_{\text{CO}}|M_{\text{PISN}}, M_{\text{BHmax}})$ given by

remnants between roughly M_{PPISN} and $M_{\text{BH,max}}$ can map back to a wider range of progenitor masses, and each BH mass bin dM_{BH} in this range contains more systems than it otherwise would had the $M_{\text{CO}} - M_{\text{BH}}$ relationship continued to be linear.

As shown in Farmer et al. (2019), the map from M_{CO} to M_{BH} is sensitive to unknown physics affecting the core collapse and stellar evolution process, even given a fixed M_{PPISN} . We therefore do not know with certainty of a one-to-one map of M_{CO} to M_{BH} and instead treat this as a probabilistic model, effectively capturing the uncertainty in physical parameters ignored in our mapping. Even if we knew global physical parameters for the core collapse process (e.g., reaction rates) with certainty, a given M_{CO} will always have a range of possible associated remnant masses due to factors such as the unknown metallicity at formation (see Sec. 3.4). Treating the M_{CO} to M_{BH} map probabilistically allows us to capture some of this uncertainty, for example, if sources from multiple metallicities are present in our

dataset, spreading out this mapping. We simulate such uncertainty in the $M_{\text{CO}} - M_{\text{BH}}$ mapping by treating the natural logarithm of the remnant mass as a realization from a Gaussian distribution, with standard deviation σ , namely

$$p(\ln(M_{\text{BH}}) | \bar{M}_{\text{BH}}, \sigma) = \mathcal{N}(\ln[\bar{M}_{\text{BH}}(M_{\text{CO}})], \sigma), \quad (4)$$

where $\bar{M}_{\text{BH}}(M_{\text{CO}})$ is given in Eq. (3). Since Eq. (4) specifies that the logarithm of M_{BH} values are normally distributed around M_{CO} with standard deviation σ , the uncertainty on the physical value of the mass M_{BH} will grow with M_{CO} for fixed σ . This is intended to be consistent with the trend in the spread around the $M_{\text{CO}} - M_{\text{BH}}$ map seen in Fig. 4 of Farmer et al. (2019), in which higher values of M_{CO} can create a larger range of remnant M_{BH} values.

Any confident measurement of a nonzero value of σ would mean there is variation in the $M_{\text{CO}} - M_{\text{BH}}$ mapping. This could originate in a number of factors, including physical properties affecting stellar evolution manifesting differently between events in the dataset. For example, since metallicity is expected to have a slight effect on the remnant mass given an initial CO core mass (Farmer et al. 2019), resolvable contributions from sources with differing birth metallicities in our dataset would result in a preferentially nonzero value for our inferred σ .

To get the resulting mass distribution for first generation BHs dN/dM_{1G} , we can simply integrate:

$$\frac{dN}{dM_{1G}}(M_{\text{BH}} | a, b, M_{\text{PPISN}}, M_{\text{BH,max}}, \sigma) = \int dM_{\text{CO}} \frac{dN}{dM_{\text{CO}}} p(M_{\text{BH}} | M_{\text{CO}}), \quad (5)$$

where we implicitly include the Jacobian from computing $p(M_{\text{BH}} | M_{\text{CO}})$ in logarithmic mass.

In Fig. 1, we show how the distribution of M_{BH} is derived from an initial distribution of CO core masses M_{CO} according to our model with some fiducial values. Each BH in the 1G population is assumed to come from a progenitor from the dN/dM_{CO} distribution (bottom panel), which is mapped to a remnant BH mass through the $M_{\text{CO}} - M_{\text{BH}}$ relationship (upper right panel). Finally, the resulting BH mass distribution dN/dM_{BH} is obtained by integrating this distribution in the upper right panel across M_{CO} , weighted by dN/dM_{CO} (Eq. 5). This differs from the procedure in Baxter et al. (2021), as we directly infer the dN/dM_{CO} and $p(M_{\text{BH}} | M_{\text{CO}})$ distributions, which uniquely specify dN/dM_{1G} rather than inferring a phenomenological representation of a resulting dN/dM_{1G} distribution.

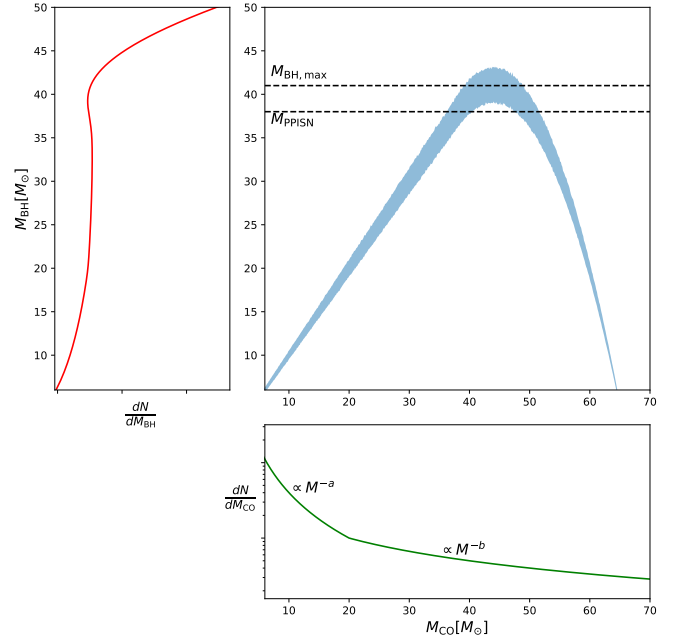


Figure 1. Obtaining a 1G BH mass distribution from the CO core IMF. The CO IMF (bottom panel) gets weighted by the M_{CO} to M_{BH} mapping (top right panel), resulting in a distribution for dN/dM_{1G} of BHs in 1G systems. We label parameters underlying the 1G BBH mass distribution: a and b are the low-mass and high-mass spectral indices of the CO IMF; M_{PPISN} and $M_{\text{BH,max}}$ (dashed lines) control the start of the nonlinear mapping and maximum of the quadratic part of the mapping, respectively. We vary these parameters in our fit to the LIGO-Virgo data, together with the parameters for the 2G population.

3.2. Full Mass Distribution

The model outlined in the previous section is only directly applicable to 1G mergers, in which M_{BH} is the remnant mass from the core collapse of one of the sources from dN/dM_{CO} . Realistically, a catalog of observed gravitational wave sources should also contain higher-generation merger events—namely, events that involve BHs who are themselves remnants of previous BH mergers—although it is commonly assumed that these systems will only subdominantly contribute to the inferred mass distribution (Miller & Hamilton 2002; Rodriguez et al. 2019; Kimball et al. 2021; Gerosa & Fishbach 2021). As the component masses of these events will be approximately (slightly less than) the sum of the masses of the BHs from its *previous* mergers, the masses in this population can exceed $M_{\text{BH,max}}$ and will not follow the same distribution as the 1G black holes.

The details of the 2G distribution depend on unknown factors that make it difficult to prescribe a specific functional form (Rodriguez et al. 2019; Kimball et al. 2021; Doctor et al. 2020). In order to capture these events in a

relatively agnostic manner, we enhance our model with a power law tail with a spectral index c that smoothly turns on just below $M_{\text{BH,max}}$, and has a height f_{pl} rel-

$$\frac{dN}{dm} = \frac{dN}{dM_{1G}} + \delta(m | M_{\text{BH,max}}) f_{pl} \left. \frac{dN}{dM_{1G}} \right|_{M_{\text{BH,max}}} \left(\frac{m}{M_{\text{BH,max}}} \right)^{-c}, \quad (6)$$

where dN/dM_{1G} is given in Eq. (5) and $\delta(m)$ is an exponential tapering function that smoothly turns on to $M_{\text{BH,max}}$; the parameter f_{pl} controls the relative height between the peak of the 2G power law and the 1G mass distribution at $M_{\text{BH,max}}$. By adopting this two-component model, we can prevent 2G sources from biasing the inference of the parameters of the dN/dM_{1G} distribution. This assumes that the 2G sources have a minimal contribution to the mass distribution below $\sim M_{\text{BH,max}}$, consistent with the conclusions from, e.g., Fishbach et al. (2022).

We model both component masses as coming from the same mass distribution dN/dM_{BH} and include a pairing function with power law slope β to get the full mass distribution:

$$\frac{dN}{dm_1 dm_2}(m_1, m_2) = (m_1 + m_2)^\beta \frac{dN}{dm_1} \frac{dN}{dm_2}, \quad (7)$$

where each $dN/dm_{1/2}$ factor corresponds to a density as in Eq. (6). The first factor in Eq. (7) constitutes the pairing function, by which the component masses do not only inform the mass distribution independently but also by how they pair together to form a total mass (Fishbach & Holz 2020; Farah et al. 2023b). The parameter β is the exponent on the total mass, such that positive (negative) values for β mean that masses pair up to preferentially form systems of higher (lower) total mass. We choose this form of the pairing function, first suggested in Fishbach & Holz (2020), to permit the possibility of *breaking* factorization symmetry, so that when $\beta \neq 0$ the joint mass function is not the product of a function of m_1 and a function of m_2 ; many of the models highlighted in LIGO Scientific Collaboration et al. (2023a) are forced to be symmetric in this sense.

Fig. 2 shows how the mass distribution dN/dm changes as a function of various population hyperparameters. The top left panel shows how M_{PPISN} predictably controls the location of the peak in the mass distribution by changing where the $M_{\text{CO}} - M_{\text{BH}}$ mapping becomes nonlinear. The upper right panel shows how this peak moves to higher M_{BH} and gets wider as $M_{\text{BH,max}}$ increases for fixed M_{PPISN} . This is due to the fact that the difference between M_{PPISN} and $M_{\text{BH,max}}$

controls the range of sources that end up in the PPISN pileup, which results in a less sharp cutoff of the pile-up as $M_{\text{BH,max}}$ increases (see, for example, the top right panel of Fig. 1 for how the quadratic turnover between M_{PPISN} and $M_{\text{BH,max}}$ causes the resulting pile-up in the BH mass distribution). The bottom left panel of Fig. 2 shows the effect of varying σ on the resulting mass distribution. As σ increases, the range of masses contributing to the pile-up widens, causing an overall smoothing of the peak. Together, these physical parameters govern the location, strength, and width of the peak in the BH mass distribution, as well as the strength of its cutoff. The final panel of Fig. 2 demonstrates the increasing contribution of the high-mass power law tail when raising f_{pl} .

3.3. Redshift Model

Studies of cosmic star formation history with astronomical surveys show that the star formation rate increases to a redshift of $z \approx 2$, then smoothly decays at high redshifts, which is well-modeled by a smoothly broken power law (Madau & Dickinson 2014; Vangioni et al. 2015; Ghirlanda et al. 2016). When convolved with a reasonable delay-time distribution, this also gives rise to a smoothly broken power law for the merger rate $R(z)$ (Fishbach et al. 2018), i.e., the number of mergers per comoving volume (V_c) per time interval in the source frame (t_s). Accordingly, we assume a redshift distribution such that

$$\frac{dN}{dV_c dt_s}(z) \equiv R(z) \propto \frac{(1+z)^\lambda}{1 + \left(\frac{1+z}{1+z_{\text{peak}}} \right)^\kappa}, \quad (8)$$

where, λ controls the low-redshift merger rate, estimated to be $\lambda \approx 3$ in current LIGO/Virgo studies (LIGO Scientific Collaboration et al. 2023a); meanwhile, the parameter z_{peak} controls the redshift at which the merger rate peaks and becomes negative. This, as well as the high-redshift merger rate, are expected to be directly informed from detections beyond the horizon of current ground-based detectors or at redshifts where detections are scarce (Callister & Farr 2023; Vitale et al. 2019; LIGO Scientific Collaboration et al. 2023a). How-

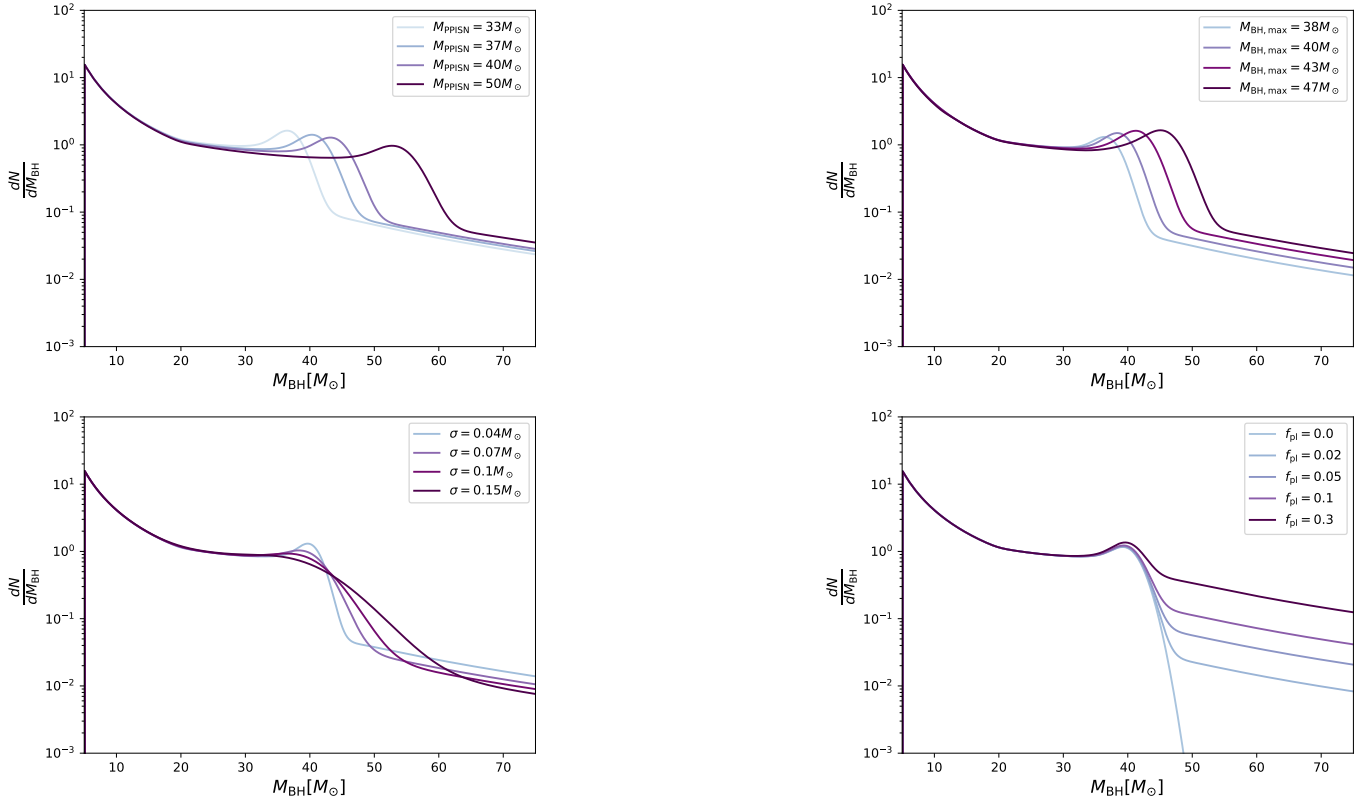


Figure 2. BH mass spectrum following our model in Eq. (7) for different choices of (clockwise from top left) M_{PPISN} , $M_{\text{BH,max}}$, f_{pl} , and σ . For the top left figure, we consider constant difference between M_{PPISN} and $M_{\text{BH,max}}$.

ever, combining upper-limits from stochastic gravitational wave searches with population inference studies can place limits on these parameters with current detections (Callister et al. 2020). Future observations with 3G detectors will allow us to significantly constrain the merger rate history across cosmic time using direct detections of BBH mergers at nearly all relevant redshifts (Ng et al. 2021; Mancarella et al. 2023).

The merger rate as a function of redshift in the detector frame is expressed simply in terms of mergers per redshift z per detector-frame time t_{det} :

$$\frac{dN}{dz dt_{\text{det}}}(z) = \frac{dN}{dV_c dt_s} \frac{dV_c}{dz} \frac{dt_s}{dt_{\text{det}}} = R(z) \frac{dV_c}{dz} \frac{1}{1+z}, \quad (9)$$

where $R(z)$ is as in Eq. (8), and dV_c/dz is the differential comoving volume per redshift bin as determined by cosmology.

3.4. Allowing the Mass Spectrum to Evolve with Redshift

Studies of stellar evolution predict that stars formed in lower-metallicity environments can reach higher remnant black hole masses before hitting the PISN cutoff. This is generally attributed to the ability for metal-rich stellar winds to carry off significant mass, resulting in

lower remnant BH masses after undergoing pulsations (Van Son et al. 2022; Marchant et al. 2019; Farmer et al. 2019). While we do not get direct information about the progenitor metallicities of gravitational-wave sources from the observed data, we can use known correlations between metallicity and observables in gravitational-wave data to look for this evolution. Redshift and metallicity are anticorrelated: stars formed earlier in the universe (i.e., at higher redshift) are relatively metal-poor when compared to those formed more recently (at lower redshift), due to the need for the existence of pre-existing stars to deposit metals into the interstellar medium in order to birth further generations of stars with higher metallicities (Maiolino et al. 2008; Belczynski et al. 2016).

Several previous studies have used this trend as motivation to search for redshift-dependence in the observed BBH mass distribution.¹ These studies have typically adopted phenomenological approaches to modeling this

¹ Van Son et al. (2022) proposes that differing delay time distributions between the high and low mass portions of the mass distribution may also result in an evolving mass distribution. Unlike evolution due to birth metallicity, this trend would not be tracked by the evolution in our model.

effect, directly encoding redshift dependence in the location of features in the BBH mass distribution. Such features include the location of the Gaussian peak and the truncation point of the mass distribution, allowing these features to vary, for example, linearly with redshift or with some function of expected metallicity at a particular redshift (Safarzadeh & Farr 2019; Fishbach et al. 2018).

We can leverage the physical framework we introduced in Sec. 3.2 to model the redshift dependence in the mapping from M_{CO} to M_{BH} . This allows us to treat the redshift evolution in the observed BBH mass distribution as a derived byproduct from an astrophysical process expected to evolve with redshift, rather than encoding the redshift dependence in the BBH mass distribution directly.

We express this evolution in term of a linear expansion for the location of the M_{PPISN} turnover in the mass distribution:

$$M_{\text{PPISN}}(z) = M_{\text{PPISN}}(z=0) + \dot{M}_{\text{PPISN}} \left(1 - \frac{1}{1+z}\right), \quad (10)$$

where M_{PPISN} and \dot{M}_{PPISN} are free parameters which we can interpret as the PPISN turnover location at $z=0$ and the change in this location over a Hubble time, respectively. This is an indirect model of the evolution of this feature from high metallicity (late universe, $z=0$) to low-metallicity (early universe, $z=\infty$) environments. One could alternatively construct a more direct model directly for M_{PPISN} as a function of metallicity and metallicity as a function of redshift.

Fig. 3 shows how our model for dN/dM_{1G} appears for different values of redshift for two choices of \dot{M}_{PPISN} . To be consistent with predictions from stellar models, as described above, we expect a positive value for \dot{M}_{PPISN} such that the turnover to PPISN occurs at higher masses at higher redshifts; equivalently, this means we expect the bump in the mass distribution moves toward higher mass at higher redshifts.

We treat the difference between M_{PPISN} and $M_{\text{BH,max}}$ as constant across redshift, such that M_{PPISN} and $M_{\text{BH,max}}$ vary together with redshift. As with the model introduced in the previous section, we include a high-mass power law tail and a pairing function for the total mass. We use the same $R(z)$ model from Sec. 3.3.

4. RESULTS

4.1. Non-Evolving Mass Distribution

Adopting the mass and redshift models introduced in the previous section, we infer the corresponding hyper-

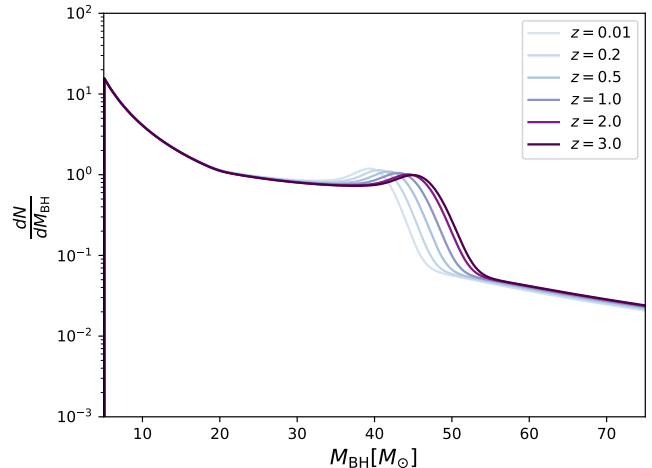


Figure 3. Model for a redshift-dependent mass distribution evaluated at selected redshifts assuming $\dot{M}_{\text{PPISN}} = 5M_{\odot}$.

parameters using the hierarchical Bayesian inference approach described in Sec. 2 and the priors in Table 4.1.

We plot draws from the mass distribution posterior in Fig. 4, which shows the inferred decaying power law shape of the mass distribution and the feature just below $\sim 40M_{\odot}$. Turning attention to the parameters that most directly control the location and strength of the peak in the mass distribution, Fig. 5 shows the posterior distributions for σ , M_{PPISN} , and $M_{\text{BH,max}}$. The recovered distribution for σ shows notable preference for low values, converging toward the lower bound of the prior ($\sigma = 0.05$). This means that the data are consistent with little to no scatter around the $M_{\text{CO}} - M_{\text{BH}}$ mapping, while ruling out high values of σ that would over-smooth the peak in the mass distribution (cf. Fig. 2, bottom panel). By the same token, the strong support for low values of σ indicates that the data do allow for a relatively sharp cutoff in the peak; this is such that a suppression of the high end of the peak need not be compensated by a higher rate in the start of the 2G tail.

With the data supporting a peak at $\sim 35M_{\odot}$, M_{PPISN} and $M_{\text{BH,max}}$ must vary together to keep the peak at the favored location (see how the peak moves with $M_{\text{BH,max}}$ in Fig. 2). This induces a strong correlation between those parameters in the corresponding 2D posterior in Fig. 5. We note that the posterior for $M_{\text{BH,max}}$ is different from the prior, indicating that the data are informing both the location and the width of the bump.

Taking the model at face value, we infer the location of $M_{\text{BH,max}}$ to be much lower than what is generally predicted by stellar nucleosynthesis simulations the corresponding beginning of the upper mass gap. For example, Farmer et al. (2019, 2020) finds the lower edge of the PISN mass gap to range between $\sim 45-50M_{\odot}$,

Parameter	Prior	Description
a	$\mathcal{N}(2.35, 2)[-1.65, 6.35]$	Power law index of low-mass CO IMF
b	$\mathcal{N}(1.9, 2)[-2.1, 5.9]$	Power law index of high-mass CO IMF
c	$\mathcal{N}(4, 2)[0, 8]$	Power law index of 2G high-mass tail
M_{PPISN}	$\mathcal{N}(35, 5)[20, 50]$	Mass at start of PPISN process [M_{\odot}]
$M_{\text{BH,max}} - M_{\text{PPISN}}$	$\mathcal{N}(3, 2)[0.5, 7]$	Maximum remnant mass produced by the 1G channel, relative to M_{PPISN} [M_{\odot}]
σ	$\mathcal{N}(0.1, 0.1)[0.05,]$	Width of lognormal distribution for M_{CO} to M_{BH} mapping
β	$\mathcal{N}(0, 2)$	Exponent on total mass pairing function
$\log(f_{\text{pl}})$	$\mathcal{U}[0.01, 0.5]$	Log of relative height between the start of the 2G powerlaw and end of dN/dM_{1G}
λ	$\mathcal{N}(2.7, 2)[-1.3, 6.7]$	Exponent controlling $R(z)$ at low redshift
$\kappa - \lambda$	$\mathcal{N}(2.9, 2)[1, 6.9]$	Exponent controlling $R(z)$ at high redshift
z_{peak}	$\mathcal{N}(1.9, 1)[0, 3.9]$	Redshift at peak $R(z)$
\dot{M}_{PPISN}	$\mathcal{U}[-2, 8]$	Difference in $M_{\text{PPISN}}(z)$ over Hubble time [M_{\odot}]

Table 1. Priors used in this work. \mathcal{U} is a uniform distribution and \mathcal{N} is a Gaussian distribution with mean and standard deviation specified in the parentheses. Numbers in square brackets are upper and lower bounds of the prior.

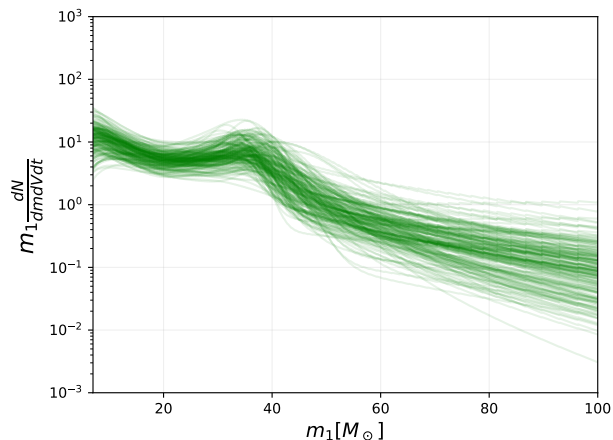


Figure 4. Draws from the mass distribution posterior, evaluated at $z = 0$.

when varying the CO reaction rate σ_{C12} within its 1σ uncertainty with respect to the distribution of reaction rates given in STARLIB (Sallaska et al. 2013). Using their fit to the start of the mass gap as a function of σ_{C12} , and extrapolating down to our inferred values of $M_{\text{BH,max}}$, we infer $\sigma_{C12} = 4.8^{+3.1}_{-2.8}$ at 90% credible levels.² Although the simulation coverage is sparse at these masses and therefore these constraints are largely extrapolation-driven, the anomalous value inferred for this parameter casts doubt on this PPISN model as a

² For reaction rates this high, the fraction of carbon in the core is too low ($X_{\text{C}} \ll 10^{-3}$) to be considered a CO core. To be consistent with the assumptions stated in Farmer et al. (2019), M_{CO} can instead be interpreted as the mass within the convective zone during helium burning.

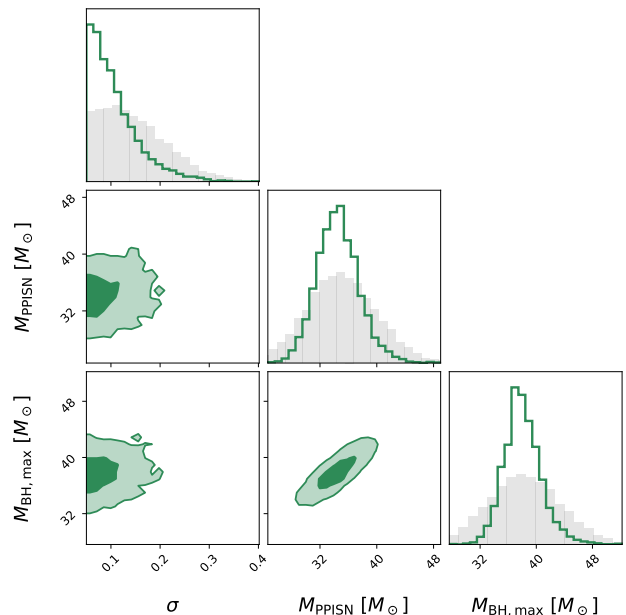


Figure 5. Posterior for selected mass distribution parameters using the model outlined in Sec. 3.2. Dark- and light-green shaded regions are the 1σ and 2σ contours, enclosing 39% and 86% of the probability respectively. Prior distribution is shaded grey for reference. We find that widening the prior does not meaningfully increase the posterior support for the PPISN feature at higher masses.

an explanation for the $\sim 35 M_{\odot}$ peak in question. See Sec. 5 for further discussion.

4.2. Evolving Mass Distribution

By adopting the more general model from Sec. 3.4 we can relax some of the assumptions made in the previous sections and now infer the mass distribution in the

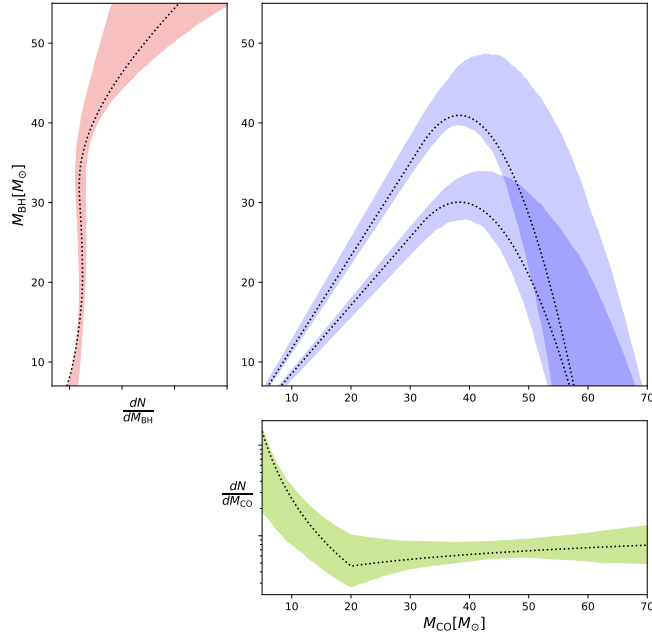


Figure 6. Representation of the $M_{\text{CO}} - M_{\text{BH}}$ relationship of the non-evolving $\frac{dN}{dM_{1G}}$ model in Sec. 3.2. (Bottom panel) Inferred distribution for the initial mass function of M_{CO} in merging binaries. (Top right panel) $1-\sigma$ credible region of the 95th percentile (higher blue shaded region) and 5th percentile (lower blue shaded region) for the inferred $M_{\text{CO}} - M_{\text{BH}}$ mapping. Dotted line is a single representative draw from the posterior.

presence of an M_{PPISN} that evolves with redshift. In Fig. 7, we present the posterior probability density on several mass distribution parameters from this model. Most of the events in the O3 catalog lie at relatively low redshift, and therefore do not provide good coverage across redshift scales to inform \dot{M}_{PPISN} meaningfully. Due to these poor constraints on \dot{M}_{PPISN} , we find that the inferred distributions for M_{PPISN} and $M_{\text{BH,max}}$ are consistent with those obtained when using the non-evolving model. In other words, the feature at M_{PPISN} is being informed by structure in the data that does not appear to need to vary with redshift. The resulting mass distribution is consistent with that which is plotted in Fig. 10.

When we extend the prior on \dot{M}_{PPISN} considerably, we find that we only rule out redshift evolution of the intrinsic mass function for very large values of \dot{M}_{PPISN} . In Fig. 9, we show the posterior distribution for relevant mass distribution parameters: constraints on \dot{M}_{PPISN} are broad, encapsulating a 90%-credible region from \dot{M}_{PPISN} from $-20 M_{\odot}$ to $36 M_{\odot}$. This range is much broader than a physical prior should allow for these parameters, as metallicity should not affect M_{PPISN} to this degree (Farmer et al. 2019). We include this for demonstration purposes; we cannot place constraints on \dot{M}_{PPISN} within a more physically-motivated restricted prior range. For the remainder of this section, we

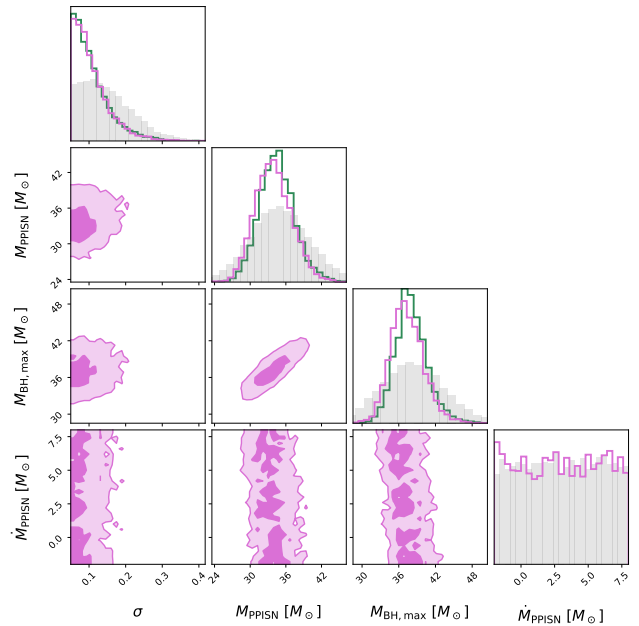


Figure 7. Posterior for selected mass distribution population parameters from the evolving mass distribution model in Sec. 3.4 (magenta). One-dimensional posteriors from the non-evolving mass model overplotted in green for reference.

present results using the narrower prior for \dot{M}_{PPISN} (in Table 4.1).

Also of note is the similarity between the distribution of σ obtained with this model and that obtained with the

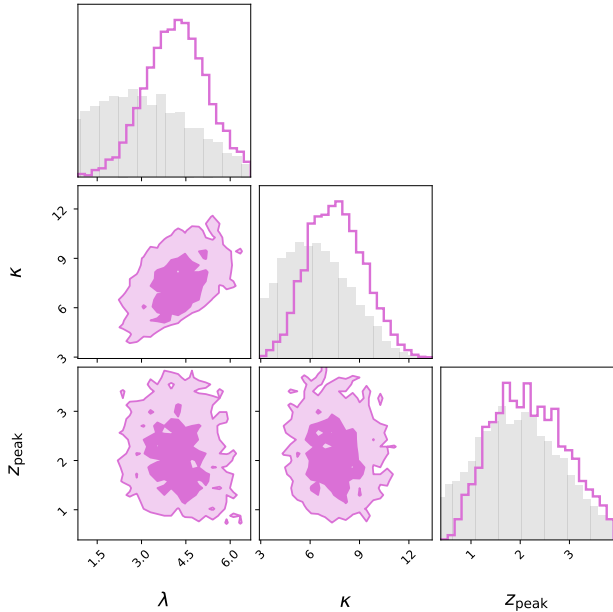


Figure 8. Redshift distribution parameters inferred with the evolving mass distribution model in Sec. 3.4. Prior distribution is shaded grey for reference.

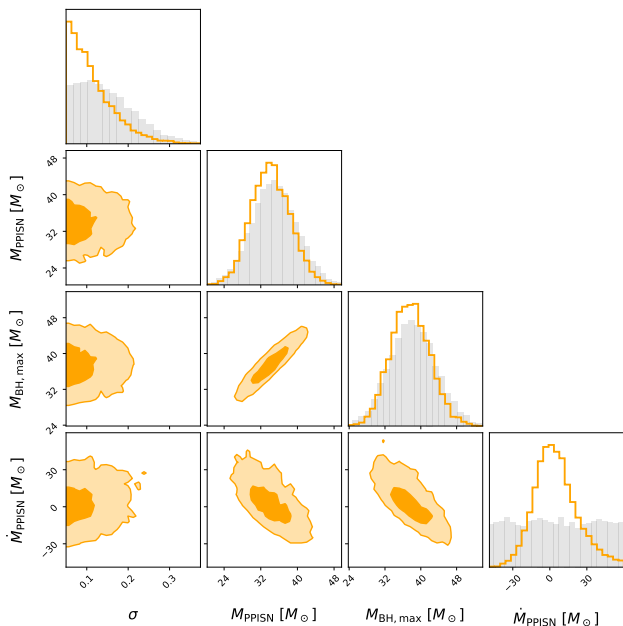


Figure 9. Inferred mass distribution parameters using the evolving mass model in Sec. 3.4, but adopting a wider prior on \dot{M}_{PPISN} . Prior distribution is shaded grey for reference.

non-evolving mass model (see the comparison in Fig. 7). We discuss the implications of this in Sec. 5.

We present the inferred redshift distribution parameters in Fig. 8. The parameter best constrained is λ , which controls the evolution of the low-redshift merger rate. We infer $\lambda = 4.3_{-1.6}^{+1.6}$, preferring a merger rate that

evolves *steeper* than the low-redshift star formation rate ($\lambda \sim 2.7$). However, the evolution of the merger rate is still consistent with that implied by the star formation rate along with a short delay-time distribution. Narrower constraints on this parameter may reveal information on different formation channels contributing to the observed catalog of BBHs.

Additionally, the posterior distribution for z_{peak} is shifted slightly to the right of the prior, meaning that we are able to begin to place very conservative lower limits on z_{peak} due to the lack of a visible start of a turnover in the inferred $R(z)$ distribution. The lack of support at the tails towards higher z_{peak} is not due to information gained from the data, but rather from the prior (see Table 4.1). These constraints appear despite having only very little high-redshift information and are therefore very weak limits.

Given the similarities between the inferred distributions with and without redshift evolution in the M_{CO} to $M_{\text{BH,max}}$ map, we do not currently obtain improved constraints on physical parameters of interest when modifying the model in this way. For example, we infer $\sigma_{C12} = 5.2_{-2.9}^{+3.4}$, which is similar to what we reported in Sec. 4.1. Future detections at higher redshift may further inform these aspects of the model.

5. INTERPRETATION OF RESULTS

By adopting the model introduced in this work, we can draw conclusions from the inferred underlying physics represented in our models and explore how the population model compares to those reported in other works.

5.1. Global Shape of the Mass Distribution

For comparison, we obtain results using the same set of O3 events, adopting the POWERLAW + PEAK mass distribution model, a flat spin magnitude and tilt model, and a broken power law redshift distribution as implemented in `gwpopulation` (Talbot et al. 2019; Talbot & Thrane 2018; Fishbach et al. 2018). Qualitatively, we infer a mass distribution (marginalized over q) consistent with the POWERLAW + PEAK model, with major features such as the slope at higher BH mass as well as the bump location showing good agreement in Fig. 10. This indicates that this overdensity is a confident feature in the data whose location and prominence is not affected by systematic differences between these two models. This is reinforced by several other works, which find that models must include such a feature in order to faithfully capture the observed mass spectrum (LIGO Scientific Collaboration et al. 2023a; Farah et al. 2023a; Edelman et al. 2022).

A notable difference we see is the relative suppression of the merger rate relative to POWERLAW + PEAK.

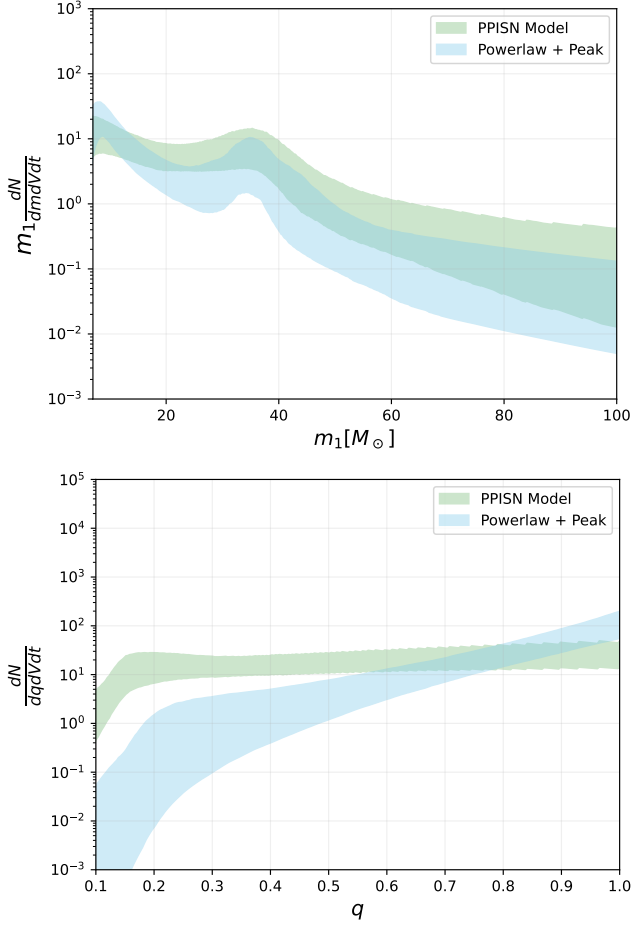


Figure 10. Mass spectrum derived from our model (green) with no evolution of the mass distribution with redshift compared to the POWERLAW + PEAK mass spectrum informed by the same events (blue). We do not include redshift evolution of the mass distribution in this comparison as the models in LIGO Scientific Collaboration et al. (2023a) do not include mass-redshift correlations. POWERLAW + PEAK results were obtained using GWPopulation (Talbot et al. 2019). (Left) Comparison of the primary mass distributions. (Right) Comparison of the mass ratio distributions.

While the 90% credible regions overlap in Fig. 10, our model tends to underestimate the merger rate with respect to the POWERLAW + PEAK model, except for at the lowest masses. While we do not know exactly the cause of the difference between the two inferred distributions, one possibility is the difference in how we reweight the component masses in the mass distribution. In our model, m_1 and m_2 both directly inform the physical mass distribution model (along with the pairing function, see Eq. 7). This is in contrast to the POWERLAW+PEAK model which has separate distributions for $p(m_1)$ and $p(q|m_1)$, such that m_2 does not directly inform dN/dm_1 . As demonstrated in Farah et al. (2023b),

this makes the mass distribution feature a peak in the joint $m_1 - m_2$ space, rather than in the marginal m_1 distribution. Furthermore, in the marginal mass ratio distribution (right panel of Fig. 10), we see that our model prefers a much flatter distribution in q than what is preferred by POWERLAW + PEAK, which explicitly models $p(q|m_1)$ as a power law. This flat mass ratio distribution is consistent with what is found in Fishbach & Holz (2020) when adopting a pairing function that is a power law in q . Given that we infer β with a preference for negative values, we find that black holes tend to pair up in binaries that favor lower total masses; this may cause a relative lack of support at higher masses in the mass distribution which models both dN/dm_1 and dN/dm_2 . We also note that the inferred local rate $R(z=0)$ is consistent between models. The POWERLAW + PEAK model fits the underlying distribution (i.e. not including the bump) with single power law, limiting the possible morphologies. We have checked that allowing the underlying power law in POWERLAW + PEAK to include a break does not resolve the discrepancy.

The distribution for $p(M_{\text{CO}})$ we infer (see Fig. 6) disagrees with what one may expect from a CO IMF resulting from the ZAMS mass IMF assuming a linear relationship between ZAMS mass and M_{CO} . While the distribution is consistent with a decaying power law for low masses, the distribution appears to flatten out above our break point of $20 M_\odot$. This trend is not strongly correlated with the M_{PPISN} and $M_{\text{BH,max}}$ we infer.

Comparing our results to those obtained in Baxter et al. (2021), we find strong tension with the maximum BH mass in the 1G channel (the start of the upper mass gap). Motivated by stellar evolution simulations to model the 1G BH mass distribution with a phenomenological approximation to the shape and location of an overdensity due to PPISN pileup, Baxter et al. (2021) finds the PPISN feature and corresponding start of the upper mass gap to be at $\sim 46 M_\odot$, in very good agreement with predictions from typical values of the $^{12}\text{C}(\alpha, \gamma)^{16}\text{O}$ reaction rate. Notably, Baxter et al. (2021) does not find the feature at $\sim 35 M_\odot$ we find and is consistently found in the literature.

5.2. Evolution of Mass Distribution with Redshift

Our finding that \dot{M}_{PPISN} is consistent with zero agrees with other studies that do not find strong preference for evolution of the BBH mass distribution with redshift. For example, Fishbach et al. (2021) models the mass distribution as a broken power law where the mass at which the power law breaks is allowed to vary with redshift. While this is a very different model, it should qualitatively reproduce some of the features of our model, par-

ticularly at the $33M_{\odot}$ feature (see Fig. 2). We therefore expect that if Fishbach et al. (2021) had found strong preferences for an evolving mass distribution, we would confidently find $\dot{M}_{\text{PPISN}} > 0$. We also agree that the data are still consistent with a mass distribution that has some evolution with redshift, but again we do not have evidence that this is the preferred scenario.

Karathanasis et al. (2023) also looks for evolution of the mass distribution with redshift. The authors allow the Gaussian bump in a POWERLAW + PEAK-like model to vary with redshift, where the placement of this peak at a given redshift is determined by the delay time distribution and a jointly-inferred model for the evolution of (birth) metallicity with redshift. The value they find for the lower edge of the upper mass gap of $\sim 44M_{\odot}$ is nominally in better agreement with the prediction from stellar physics models. However, this value is cited at low metallicity, and they also find there must be a very strong evolution of this mass scale with metallicity. Extrapolating their results to the local universe, they find that the upper mass gap at $z = 0$ starts at $\sim 30M_{\odot}$, which is closer to the corresponding value we obtain for the start of the $M_{\text{CO}} - M_{\text{BH}}$ turnover. This result seems in tension with theoretical predictions given how small of an effect metallicity is expected to have on M_{PPISN} . There are unexplained differences in our results, however, as such a strong evolution of M_{PPISN} with metallicity should mean that we would infer a positive \dot{M}_{PPISN} , assuming delays do not mix events from many different birth metallicities into similar merger times.

If metallicity evolution effects were causing some of the support for nonzero values of σ obtained in the non-evolving mass model (i.e., from scatter in the $M_{\text{CO}} - M_{\text{BH}}$ relation), we would expect σ to be constrained closer to zero with the evolving model, as some of that scatter would have been absorbed by the redshift evolution. Given that this is not the case, we conclude that either (1) birth metallicity effects fundamentally have a subdominant impact on the $M_{\text{CO}} - M_{\text{BH}}$ relationship compared to other physical parameters that vary between BBH systems, or that (2) the birth metallicities of the systems in our catalog are not strongly correlated with the redshifts at which they merge. The latter scenario could result from the delay time distribution between formation and merger having enough support in the long-delay tails such that we cannot yet discern a strong correlation between birth time and merger redshift for systems merging at redshifts of $z \lesssim 1$.

5.3. Physical Interpretations

5.3.1. PPISN Process

We can also take advantage of the underlying physical parameterization of our model and offer corresponding interpretations of the implied stellar physics, assuming $M_{\text{BH,max}}$ corresponds to the maximum 1G BH mass as determined by the PPISN process at a given redshift/metallicity. As found in several simulation-based studies, the $^{12}\text{C}(\alpha, \gamma)^{16}\text{O}$ reaction rate is most important reasonably-tunable physical parameter for determining the maximum BH mass (Farmer et al. 2020; Mehta et al. 2022; Farag et al. 2022). We therefore consider the $^{12}\text{C}(\alpha, \gamma)^{16}\text{O}$ reaction rate to be the dominant unknown physical parameter leading to the measured value of $M_{\text{BH,max}}$. Under this assumption, Fig. 11 shows the fit for maximum BH mass as a function of σ_{C12} (each corresponding to a different value of the $^{12}\text{C}(\alpha, \gamma)^{16}\text{O}$ rate) from the MESA simulations in Farmer et al. (2020) (reproduced from their data release). While their simulations only cover the range $-3 < \sigma_{\text{C12}} < 3$, there is a clear trend that σ_{C12} must rise very steeply to reach values of maximum BH mass below $\sim 45M_{\odot}$.³

With the core temperature strongly increasing with stellar mass, there exists a core mass at which the softening of the equation of state is too extreme to be resisted by available sources outward pressure. Since stable outward pressure support at this stage is largely provided by shell carbon-burning, the lower carbon fraction, X_{C} , makes it now easier for a given contraction to compress and fully ignite the oxygen core, driving a subsequent pulsation so powerful that further pair production in the core cannot re-soften the equation of state fast enough to return it to a contraction phase. This is basically equivalent to a single pulsation during the pulsational pair-instability process blowing away the total mass of the star (Woosley 2017, 2019; Woosley & Heger 2021). A lower carbon fraction results in this full disruption of

³ The physical reason for this trend is that during contraction of the stellar core, hydrostatic equilibrium can be maintained by convective carbon burning. Higher $^{12}\text{C}(\alpha, \gamma)^{16}\text{O}$ reaction rates lead to cores of lower carbon fractions, X_{C} . When the core gets hot enough to produce electron-positron pairs, the equation of state softens, leading to a contraction. With little carbon present to provide convective-driven pressure to stabilize the star, contraction can continue until it drives thermonuclear ignition of oxygen. This explosive process leads to an outward-moving shock, removing mass from the star when the shock reaches the surface with enough velocity. Once this shock breaks through the surface of the star, contraction begins again. This sequence of pulsations continues until oxygen in the core is depleted, core elements burn through the normal pre-SN process, and the star undergoes normal core collapse. If the $^{12}\text{C}(\alpha, \gamma)^{16}\text{O}$ reaction rate is lower, then relatively more carbon is present and able to burn convectively, counteracting the contractions in a stable manner. As the carbon fraction gets higher, the star is able to remain stable against pair-production contractions and stably burn through the core oxygen (Farmer et al. 2020; Woosley 2017, 2019)

the star (PISN) occurring at lower masses, controlling where the $M_{\text{CO}} - M_{\text{BH}}$ map decays to 0 after $M_{\text{BH,max}}$.

5.3.2. Implications for PPISN Physics

Each value of σ_{C12} corresponds to a different $^{12}\text{C}(\alpha, \gamma)^{16}\text{O}$ reaction rate, where σ_{C12} is the number of standard deviations from the median of the distribution of reaction rates given in STARLIB (Sallaska et al. 2013) (which is adopted from (Kunz et al. 2002)) and is the distribution of reaction rates used in the MESA simulations in Farmer et al. (2020). After fitting for the σ_{C12} values necessary to give the $M_{\text{BH,max}}$ values we infer, we use the method suggested in Farmer et al. (2020) to approximate these reaction rates to S-factors for the $^{12}\text{C}(\alpha, \gamma)^{16}\text{O}$ reaction.⁴ We arrive at a value of the S-factor at 300 keV of $S_{300} = 932^{+1929}_{-581}$ keV · barn.

In Fig. 11, we compare this estimate of S_{300} to that which is reported in deBoer et al. (2017), in which the authors aggregate a large catalog of experimental studies related to the $^{12}\text{C}(\alpha, \gamma)^{16}\text{O}$ cross-section and use numerical methods to extrapolate to an estimated low-energy S-factor. That value is in strong tension with respect to our estimate: our estimate rules out the value from deBoer et al. (2017) at > 99.9% credibility. This is in contrast with Farag et al. (2022) and Farmer et al. (2020), which present inferred values or lower limits of S_{300} which are consistent with the predicted value. However, these studies draw these conclusions assuming that S_{300} can be inferred from the most massive black holes in the observed catalog, assuming that individual high-mass events are 1G BBH mergers. In contrast, we infer the entire astrophysical mass distribution, with a subpopulation of 1G BHs that cuts off at a mass by determined the inferred location and strength of the turnover in the $M_{\text{CO}} - M_{\text{BH}}$ mapping. We furthermore allow for high-mass events to belong to a separate 2G BBH subpopulation that contaminates the 1G upper mass gap, inferring $M_{\text{BH,max}}$ to be where the 1G BBH subpopu-

⁴ While the total reaction rate is given by the cross-section, it is common in the stellar nuclear physics literature to characterize it in terms of the so-called ‘‘astrophysical S-factor’’. This factor can be thought of as the part of the cross section that is given by the matrix element for the nuclear reaction itself, ignoring Coulomb repulsion effects between nuclei. At the (relatively low) typical energies for this reaction in the relevant phase of stellar evolution ($E \sim 300\text{keV}$), the effects from the Coulomb repulsion between the positively-charged ^{12}C and α nuclei exponentially suppresses the cross-section. It is therefore sometimes convenient to express the cross-section in terms of the product of two distinct factors: the S-factor for the reaction, which varies slowly with energy, and the Gamow factor which characterizes the tunneling probability through the Coulomb barrier and gives exponential suppression of the cross section at low energies (see Kippenhahn & Weigert (1994))

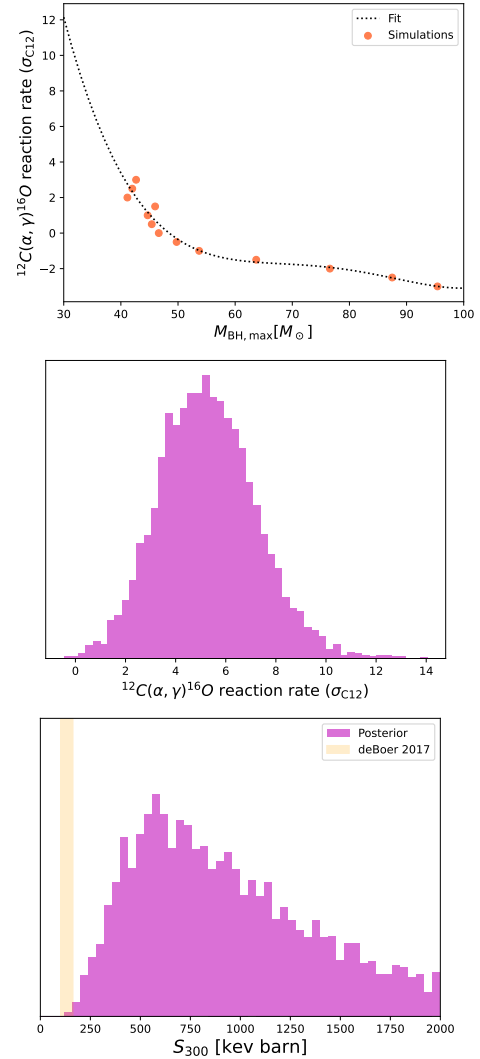


Figure 11. (Top) Relationship between σ_{C12} and lower edge of upper mass gap, reproduced from data release of Farmer et al. (2020). (Center) Posterior distribution of $^{12}\text{C}(\alpha, \gamma)^{16}\text{O}$ reaction rate, in terms of standard deviations away from the median reaction rate in STARLIB (Sallaska et al. 2013); computed by evaluating the fit in the top left for the samples of $M_{\text{BH,max}}$ in the posterior. (Bottom) Inferred distribution of S_{300} , extrapolated from distribution of σ_{C12} as calculated from the fit in the left panel. Constraints on S_{300} from deBoer et al. (2017) plotted for comparison, showing tension with the values implied from our results.

lation ends, therefore leading to a lower inferred lower edge of the upper mass gap. Given the confidence with which the values of S_{300} reported in the nuclear physics literature lie below what we report, we conclude that one of the assumptions we make when calculating S_{300} from our inferred mass distribution is incorrect.

One assumption in this calculation is that the $^{12}\text{C}(\alpha, \gamma)^{16}\text{O}$ reaction rate is the dominant physical parameter controlling the location of $M_{\text{BH,max}}$. While

neglecting the uncertainty from other nuclear reaction rates certainly causes some sort of bias when we infer S_{300} , such a bias is likely too weak to result in the tension we see, as multiple studies find that varying the $^{12}\text{C}(\alpha, \gamma)^{16}\text{O}$ reaction rate has a much stronger effect on the location of the start of the upper mass gap than other relevant reaction rates (i.e. 3α , $^{12}\text{C} + ^{12}\text{C}$, $^{12}\text{C} + ^{16}\text{O}$, and $^{16}\text{O} + ^{16}\text{O}$) (Farmer et al. 2020; Farag et al. 2022). The caveat here again is that these simulations only go up to a maximum reaction rate of $\sigma_{C12} = 3$ with respect to the reaction rate distribution in STARLIB Sallaska et al. (2013), so we cannot confirm the effect of varying these other reactions rates when σ_{C12} is high (let alone the predicted lower edge of the upper mass gap for these reaction rates, for which we must extrapolate beyond the simulation space of reaction rates). While it is possible that one of these other reaction rates can be varied within their uncertainties to allow us to infer a lower σ_{C12} , it would have to change the location of the upper mass gap substantially to agree with the data; again, studies currently in the literature indicate that these reaction rates do not have such a strong effect (Farmer et al. 2019; Farag et al. 2022; Woosley & Heger 2021).

Another assumption we make is that the simulations which inspire our model accurately represent the $M_{\text{CO}} - M_{\text{BH}}$ mapping for a fixed $^{12}\text{C}(\alpha, \gamma)^{16}\text{O}$ reaction rate. Mass-loss prescriptions and temporal resolutions of the simulations (particularly given the high σ_{C12} we wish to probe) may introduce an unknown bias into the assumptions we make when associating the inferred $M_{\text{CO}} - M_{\text{BH}}$ mapping with an underlying physical parameter (Mehta et al. 2022; Farag et al. 2022; Farmer et al. 2019). Again, from the set of simulations presented in the literature, varying these settings have a subdominant impact on the location of the upper mass gap.

A final strong assumption we make is in this interpretation is that the turnover in the $M_{\text{CO}} - M_{\text{BH}}$ mapping can in fact be associated with the pair-instability process at all. Studies have suggested that associating the observed peak in the mass distribution with the PPISN pileup is in tension with known stellar physics and observed supernovae rates (Hendriks et al. 2023; Woosley & Heger 2021). Inferring the underlying $M_{\text{CO}} - M_{\text{BH}}$ mapping that gives rise to the observed BH mass distribution, this work also provides evidence of such a tension in terms of the underlying physics that would be necessary to generate a turnover in the $M_{\text{CO}} - M_{\text{BH}}$ map at the correct location.

The cause of the peak in the observed mass distribution at $\sim 35M_{\odot}$ therefore requires alternative explana-

tions (Hendriks et al. 2023). Recent studies have proposed that this overdensity could be a signature from a subpopulation of binaries which had undergone stable mass transfer (Briel et al. 2023), BBH systems in globular clusters (Antonini et al. 2023), and stars which have undergone significant wind-driven mass loss. The model introduced in this work may be relevant to describe any mechanism that generates a peak in the high-mass tail of the 1G mass distribution via a transition to a nonlinear $M_{\text{CO}} - M_{\text{BH}}$ relationship.

5.4. Model Limitations

Our model has a few caveats that may affect our results. For example, our model does not attempt to fit for the features that we know exist at lower masses beyond a power law (Edelman et al. 2022; LIGO Scientific Collaboration et al. 2023a; Farah et al. 2023a). We have confirmed that neglecting this does not bias the inference in the higher-mass region that we care about here, and this will be explored in future work. We also ignore the effect of spins in our population, but we demonstrate in Appendix B that this does not cause a notable bias in our results of interest. Given that certain mass-spin correlations have been found in the BBH population (Callister et al. 2021), it may be insightful to use the spins to help distinguish the 1G and 2G subpopulations (see, e.g., Fishbach et al. (2017); Gerosa & Berti (2017); Farr et al. (2017)).

6. CONCLUSIONS

Characterizing the population of BBH masses with direct phenomenological or nonparametric fits can provide insight into the shape of the mass distribution, but does not provide direct constraints on the underlying physics of BBH masses. With the method we propose, we can infer the underlying physics by fitting the implied (derived) astrophysical distribution to the observed data. We demonstrate the use of this method by evaluating the role of the PPISN process giving rise to the 1G mass distribution and creating a bump in the mass distribution, finding that the necessary physical parameters are unrealistic from a nuclear physics perspective. We therefore conclude it is highly unlikely that the feature at $\sim 35M_{\odot}$ is associated with the PPISN process.

This framework motivates future investigations to better constrain the physics underlying astrophysical populations in general. Future work using additional observations may be able to constrain proposed astrophysical mechanisms underpinning the BBH mass, spin, and redshift distributions using similar approaches. This approach may offer fruitful applications such as calibration of “spectral siren” features for cosmology (Farr et al.

2019), investigating other proposed interpretations of the bumps in the mass distribution, and understanding progenitor populations by relating back to population synthesis configurations (Wong et al. 2023; Andrews et al. 2021; Zevin et al. 2017).

ACKNOWLEDGEMENTS

We thank Mathieu Renzo for helpful discussions about MESA simulations and the physics of stellar evolution and the PPISN process. We also acknowledge Alan Weinstein for useful comments and discussions, and Maya Fishbach for helpful comments on the manuscript. The Flatiron Institute is a division of the Simons Foundation. The authors are grateful for computational resources provided by the LIGO Lab and supported by National Science Foundation Grants PHY-0757058 and PHY-0823459. JG is supported by NSF award No. 2207758. This research has made use of data or software obtained from the Gravitational Wave Open Science Center (gwosc.org), a service of the LIGO Scientific Collaboration, the Virgo Collaboration, and KAGRA.

This material is based upon work supported by NSF’s LIGO Laboratory which is a major facility fully funded by the National Science Foundation, as well as the Science and Technology Facilities Council (STFC) of the United Kingdom, the Max-Planck-Society (MPS), and the State of Niedersachsen/Germany for support of the construction of Advanced LIGO and construction and operation of the GEO600 detector. Additional support for Advanced LIGO was provided by the Australian Research Council. Virgo is funded, through the European Gravitational Observatory (EGO), by the French Centre National de Recherche Scientifique (CNRS), the Italian Istituto Nazionale di Fisica Nucleare (INFN) and the Dutch Nikhef, with contributions by institutions from Belgium, Germany, Greece, Hungary, Ireland, Japan, Monaco, Poland, Portugal, Spain. KAGRA is supported by Ministry of Education, Culture, Sports, Science and Technology (MEXT), Japan Society for the Promotion of Science (JSPS) in Japan; National Research Foundation (NRF) and Ministry of Science and ICT (MSIT) in Korea; Academia Sinica (AS) and National Science and Technology Council (NSTC) in Taiwan.

APPENDIX

A. DETAILS OF THE LIKELIHOOD AND DIFFERENTIAL RATE CALCULATION

Setting θ to be the set of single-event parameters, we can write the contribution from i th-event to the population likelihood as (Mandel et al. 2019):

$$p(d_i|\Lambda) = \frac{\int d\theta_i p(d_i|\theta_i) p(\theta_i|\Lambda) p_{\text{det}}(\theta_i, d_i)}{\int \int dd_i d\theta_i p(d_i|\theta_i) p(\theta_i|\Lambda) p_{\text{det}}(\theta_i, d_i)} \quad (\text{A1})$$

Recalling that the probability density should be normalized over the arguments on the left side of the bar, the denominator is included to explicitly normalize the numerator in terms of the data from the i th detection, and is commonly known as the “selection effects” term. We write the detection probability as $p_{\text{det}}(\theta_i, d_i)$ in order to include the general possibility of thresholding detection in terms of the event parameters, which may be implemented when considering, for example, a simulated catalog. For our purposes, the detection probability depends on the data, as this is the input to a detection pipeline when assigning a FAR. The normalization in the denominator also corresponds to the fraction of detectable events expected from the population given by Λ (Farr 2019). We make the following definition of the denominator:

$$\mu(\Lambda) \equiv \int \int dd_i d\theta_i p(d_i|\theta_i) p(\theta_i|\Lambda) p_{\text{det}}(\theta_i, d_i) \quad (\text{A2})$$

The total likelihood comes from considering the probability of the entire dataset $\{d_i\}$ of N_d detections (where the i th event is detected if p_{det} is 1), given a population with parameters Λ that predicts N total events, $N\mu \equiv K(\Lambda)$ of which are expected to be detected. The total likelihood is just the product of the contributions from all the detected events, and the likelihood of detecting N_d events, considering the realization of N_d comes from a Poisson distribution with expected value K :

$$p(\{d\}|\Lambda, K) = p(N_d|K(\Lambda)) \prod_i^{N_d} p(d_i|\Lambda) \propto K(\Lambda)^{N_d} e^{-K(\Lambda)} \mu(\Lambda)^{-N_d} \prod_i^{N_d} \int d\theta_i p(d_i|\theta_i) p(\theta_i|\Lambda). \quad (\text{A3})$$

If we assume a prior of $\pi(K) \propto 1/K$, we can write the posterior over Λ and analytically integrate out the distribution over K :

$$\begin{aligned}
p(\Lambda|\{d\}) &\propto \pi(\Lambda) \int dK \frac{K(\Lambda)^{N_d} e^{-K(\Lambda)}}{K} \mu(\Lambda)^{-N_d} \prod_i^{N_d} \int d\theta_i p(d_i|\theta_i) p(\theta_i|\Lambda) \\
&= \Gamma(N_d) \pi(\Lambda) \mu(\Lambda)^{-N_d} \prod_i^{N_d} \int d\theta_i p(d_i|\theta_i) p(\theta_i|\Lambda) \\
&\propto \pi(\Lambda) \mu(\Lambda)^{-N_d} \prod_i^{N_d} \int d\theta_i p(d_i|\theta_i) p(\theta_i|\Lambda)
\end{aligned} \tag{A4}$$

where $\Gamma(N_d)$ does not depend on Λ , so marginalizing over $K(\Lambda)$ with this choice of $\pi(K)$ allows us to factorize the above equation, without explicitly considering its dependence on the Poisson term.

In practice, $p(\theta|\Lambda)$ does not need to be normalized, as any prefactors will divide out in Eq. A1. We therefore only need to calculate something proportional to $p(\theta|\Lambda)$. For reasons that will become apparent, we compute $p(\theta|\Lambda)$ in terms of something proportional to $\frac{dN}{d\theta}(\Lambda)$. We want to define a normalization factor for the population distribution such that:

$$\frac{1}{\alpha(\Lambda)} m_1 \frac{dN}{dm_1 dq dV dt_s} \Big|_{(m_{\text{ref}}, q_{\text{ref}}, z_{\text{ref}})} = 1 \tag{A5}$$

where the differential rate is evaluated at a set of reference parameters.

With the distributions in Sec. 3 defined in terms of $\frac{dN}{dm}$ and $\frac{dN}{dV dt_s}$ (i.e. source frame merger rate density $\mathcal{R}(z)$), we can compute a normalization factor $\alpha(\Lambda)$:

$$\begin{aligned}
\alpha(\Lambda) &= m_1 \frac{dN}{dm_1 dq dV dt_s}(\Lambda) \Big|_{(m_{\text{ref}}, q_{\text{ref}}, z_{\text{ref}})} = m_1 \frac{dN}{dm_1} \frac{dN}{dm_2} \frac{dm_2}{dq} \frac{dN}{dV dt_s} \Big|_{(m_{\text{ref}}, q_{\text{ref}}, z_{\text{ref}})} \\
&= m_1^2 \frac{dN}{dm} \frac{dN}{dm} \frac{dN}{dV dt_s} \Big|_{(m_{\text{ref}}, q_{\text{ref}}, z_{\text{ref}})}
\end{aligned} \tag{A6}$$

Technically, we only know the dN distributions up to a constant. As we will see below, we will only be considering ratios of values that share the same unknown constant, so we are free to leave it out for now.

Instead of computing $p(\theta|\Lambda)$ as $p(\theta|\Lambda) = \frac{1}{N} \frac{dN}{d\theta}(\Lambda)$ exactly, we instead make the following transformation in Equations A1 and A4:

$$p(\theta|\Lambda) \rightarrow \frac{1}{\alpha(\Lambda)} \frac{dN}{d\theta}(\Lambda) \tag{A7}$$

which is directly proportional to the differential rate and $p(\theta|\Lambda)$.

For each draw of Λ , we have the normalization factor $\alpha(\Lambda)$, related to the differential rate at our reference parameters, as defined in Eq. A6. We outline below how we use this re-expression to construct the rate independent of the likelihood. Note that this change in Eq. A7 does not affect the likelihood, as it only affects θ -independent prefactors, which factor out of both the numerator and denominator in Eq. A1.

Given the values of $\alpha(\Lambda)$ we have calculated, we wish to draw samples new samples of $\alpha(\Lambda)$, given the number of detections is a Poisson-distributed realization. Recalling $K \equiv N\mu$, Eq. A7 means that when we compute the denominator of Eq. A1, we are actually calculating the ratio $\frac{K}{\alpha}$, and not μ . Noting that the K-dependent integrand of Eq. A4 is a Gamma-distribution for K with shape parameter N_d and a scale parameter of 1, we can make the identification that $\langle K \rangle = N_d$ under this distribution. With $K \equiv N\mu$, we can express the expectation value for α as $\langle \alpha \rangle = \frac{N_d}{K/\alpha}$.⁵ As a final step in post-processing, we can construct the true underlying distribution for α by drawing samples $\alpha \sim \text{Gamma}(\frac{N_d}{K/\alpha}, 1)$. This gives us a distribution for the predicted merger rate at the reference coordinates, given the normalization factor α we computed during the hierarchical inference, assuming this is Poisson-distributed about the true value and assuming a $\frac{1}{K}$ prior. With the distribution of α , we can scale $\frac{dN}{d\theta}$ to get the differential merger rate at any set of coordinates θ .

⁵ Since $\langle K \rangle = N_d$, it follows that $\sigma_\alpha^2 = \frac{N_d}{(K/\alpha)^2}$

Note that we have written everything in this section in terms of θ as if it is always the parameters in the population model, suppressing the fact that there will be Jacobians in Eq. A1 to transform from these coordinates to those in the detector-frame (or the priors from the single-event analyses).

B. ACCOUNTING FOR SPIN DISTRIBUTION

In the analysis presented in the body of this work, we assume the (uninformative) parameter estimation priors in the population reweighting. Based on population-level mass-spin and mass-redshift correlations presented in the literature (see, e.g., Callister et al. (2021); Biscoveanu et al. (2022); LIGO Scientific Collaboration et al. (2023a)), we may expect the assumed spin distribution can have an effect on our results. However, with the relatively poor spin constraints in the population, we empirically demonstrate that this is likely not the case.

In Figure 12, we compare posteriors obtained from our main analysis ignoring spins, with those obtained by reweighting the posterior samples from each event and the sensitivity injections to a fiducial spin distribution. For this fiducial spin distribution, the spin magnitudes are from a half-Gaussian centered at $a = 0$ with a standard deviation of 0.3, meant to model the preferentially-small spin magnitudes inferred in LIGO Scientific Collaboration et al. (2023a). For the contribution aligned projection of the spin tilt angle ($\cos\theta$), we use the mixture model introduced in Talbot & Thrane (2017), with an aligned-spin fraction of $\xi = 0.8$ and an aligned-spin spread of $\sigma_t = 1.9$, consistent with the results reported in LIGO Scientific Collaboration et al. (2023a) (see references for definitions of these model parameters). We find that reweighting to this spin distribution has a negligible effect on our inferred population.

REFERENCES

- Aasi, J., et al. 2015, *Class. Quant. Grav.*, 32, 074001, doi: [10.1088/0264-9381/32/7/074001](https://doi.org/10.1088/0264-9381/32/7/074001)
- Abbott, B. P., et al. 2018, *Living Rev. Rel.*, 21, 3, doi: [10.1007/s41114-020-00026-9](https://doi.org/10.1007/s41114-020-00026-9)
- Abbott, R., et al. 2021. <https://arxiv.org/abs/2112.06861>
- Acernese, F., et al. 2015, *Class. Quant. Grav.*, 32, 024001, doi: [10.1088/0264-9381/32/2/024001](https://doi.org/10.1088/0264-9381/32/2/024001)
- Andrews, J. J., Cronin, J., Kalogera, V., Berry, C. P. L., & Zezas, A. 2021, *ApJL*, 914, L32, doi: [10.3847/2041-8213/ac00a6](https://doi.org/10.3847/2041-8213/ac00a6)
- Antonini, F., Gieles, M., Dosopoulou, F., & Chattopadhyay, D. 2023, *Monthly Notices of the Royal Astronomical Society*, 522, 466–476, doi: [10.1093/mnras/stad972](https://doi.org/10.1093/mnras/stad972)
- Baxter, E. J., Croon, D., McDermott, S. D., & Sakstein, J. 2021, *ApJL*, 916, L16, doi: [10.3847/2041-8213/ac11fc](https://doi.org/10.3847/2041-8213/ac11fc)
- Belczynski, K., Holz, D. E., Bulik, T., & O’Shaughnessy, R. 2016, *Nature*, 534, 512
- Bingham, E., Chen, J. P., Jankowiak, M., et al. 2019, *J. Mach. Learn. Res.*, 20, 28:1. <http://jmlr.org/papers/v20/18-403.html>
- Biscoveanu, S., Callister, T. A., Haster, C.-J., et al. 2022, *ApJL*, 932, L19, doi: [10.3847/2041-8213/ac71a8](https://doi.org/10.3847/2041-8213/ac71a8)
- Bradbury, J., Frostig, R., Hawkins, P., et al. 2018, JAX: composable transformations of Python+NumPy programs, 0.3.13. <http://github.com/google/jax>
- Briel, M. M., Stevance, H. F., & Eldridge, J. J. 2023, *Monthly Notices of the Royal Astronomical Society*, 520, 5724–5745, doi: [10.1093/mnras/stad399](https://doi.org/10.1093/mnras/stad399)
- Callister, T., Fishbach, M., Holz, D. E., & Farr, W. M. 2020, *ApJL*, 896, L32, doi: [10.3847/2041-8213/ab9743](https://doi.org/10.3847/2041-8213/ab9743)
- Callister, T. A., & Farr, W. M. 2023, arXiv e-prints, arXiv:2302.07289, doi: [10.48550/arXiv.2302.07289](https://doi.org/10.48550/arXiv.2302.07289)
- Callister, T. A., Haster, C.-J., Ng, K. K. Y., Vitale, S., & Farr, W. M. 2021, *ApJL*, 922, L5, doi: [10.3847/2041-8213/ac2ccc](https://doi.org/10.3847/2041-8213/ac2ccc)
- deBoer, R., Görres, J., Wiescher, M., et al. 2017, *Reviews of Modern Physics*, 89, 035007, doi: [10.1103/RevModPhys.89.035007](https://doi.org/10.1103/RevModPhys.89.035007)
- Doctor, Z., Wysocki, D., O’Shaughnessy, R., Holz, D. E., & Farr, B. 2020, *The Astrophysical Journal*, 893, 35
- Duane, S., Kennedy, A. D., Pendleton, B. J., & Roweth, D. 1987, *Physics Letters B*, 195, 216–222, doi: [https://doi.org/10.1016/0370-2693\(87\)91197-X](https://doi.org/10.1016/0370-2693(87)91197-X)
- Edelman, B., Doctor, Z., Godfrey, J., & Farr, B. 2022, *ApJ*, 924, 101, doi: [10.3847/1538-4357/ac3667](https://doi.org/10.3847/1538-4357/ac3667)
- Ezquiaga, J. M., & Holz, D. E. 2022, *PhRvL*, 129, 061102, doi: [10.1103/PhysRevLett.129.061102](https://doi.org/10.1103/PhysRevLett.129.061102)
- Farag, E., Renzo, M., Farmer, R., Chidester, M. T., & Timmes, F. X. 2022, *The Astrophysical Journal*, 937, 112, doi: [10.3847/1538-4357/ac8b83](https://doi.org/10.3847/1538-4357/ac8b83)
- Farah, A. M., Edelman, B., Zevin, M., et al. 2023a, arXiv e-prints, arXiv:2301.00834, doi: [10.48550/arXiv.2301.00834](https://doi.org/10.48550/arXiv.2301.00834)
- Farah, A. M., Fishbach, M., & Holz, D. E. 2023b, arXiv e-prints, arXiv:2308.05102, doi: [10.48550/arXiv.2308.05102](https://doi.org/10.48550/arXiv.2308.05102)
- Farmer, R., Renzo, M., de Mink, S., Fishbach, M., & Justham, S. 2020, *The Astrophysical Journal*, 902, L36, doi: [10.3847/2041-8213/abbadd](https://doi.org/10.3847/2041-8213/abbadd)

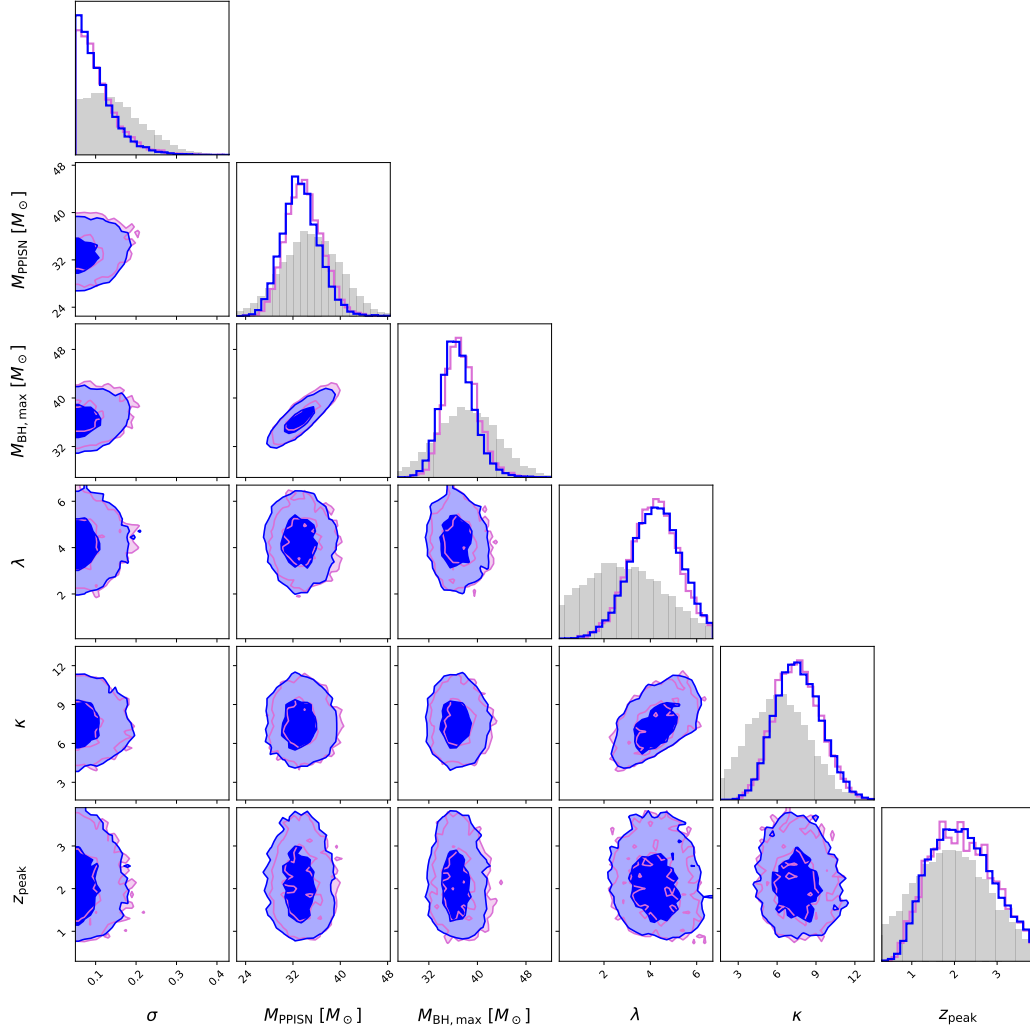


Figure 12. Selected population-level parameters from the evolving mass distribution analysis, without reweighting spins (pink, as presented in Section 4.2) and with reweighting spins to a fiducial population estimate (blue). The near-identical posteriors show that the spin population assumptions in this work do not cause a bias.

Farmer, R., Renzo, M., De Mink, S. E., Marchant, P., & Justham, S. 2019, *The Astrophysical Journal*, 887, 53, doi: [10.3847/1538-4357/ab518b](https://doi.org/10.3847/1538-4357/ab518b)

Farr, W. M. 2019, *Research Notes of the American Astronomical Society*, 3, 66, doi: [10.3847/2515-5172/ab1d5f](https://doi.org/10.3847/2515-5172/ab1d5f)

Farr, W. M., Fishbach, M., Ye, J., & Holz, D. E. 2019, *ApJL*, 883, L42, doi: [10.3847/2041-8213/ab4284](https://doi.org/10.3847/2041-8213/ab4284)

Farr, W. M., Stevenson, S., Miller, M. C., et al. 2017, *Nature*, 548, 426–429, doi: [10.1038/nature23453](https://doi.org/10.1038/nature23453)

Fishbach, M., & Holz, D. E. 2017, *ApJL*, 851, L25, doi: [10.3847/2041-8213/aa9bf6](https://doi.org/10.3847/2041-8213/aa9bf6)

—. 2020, *ApJL*, 891, L27, doi: [10.3847/2041-8213/ab7247](https://doi.org/10.3847/2041-8213/ab7247)

Fishbach, M., Holz, D. E., & Farr, B. 2017, *ApJL*, 840, L24, doi: [10.3847/2041-8213/aa7045](https://doi.org/10.3847/2041-8213/aa7045)

Fishbach, M., Holz, D. E., & Farr, W. M. 2018, *The Astrophysical Journal*, 863, L41, doi: [10.3847/2041-8213/aad800](https://doi.org/10.3847/2041-8213/aad800)

Fishbach, M., Kimball, C., & Kalogera, V. 2022, *ApJL*, 935, L26, doi: [10.3847/2041-8213/ac86c4](https://doi.org/10.3847/2041-8213/ac86c4)

Fishbach, M., & van Son, L. 2023, *ApJL*, 957, L31, doi: [10.3847/2041-8213/ad0560](https://doi.org/10.3847/2041-8213/ad0560)

Fishbach, M., Doctor, Z., Callister, T., et al. 2021, *The Astrophysical Journal*, 912, 98, doi: [10.3847/1538-4357/abee11](https://doi.org/10.3847/1538-4357/abee11)

Fowler, W. A., & Hoyle, F. 1964, *ApJS*, 9, 201, doi: [10.1086/190103](https://doi.org/10.1086/190103)

Gerosa, D., & Berti, E. 2017, *PhRvD*, 95, 124046, doi: [10.1103/PhysRevD.95.124046](https://doi.org/10.1103/PhysRevD.95.124046)

Gerosa, D., & Fishbach, M. 2021, *Nature Astronomy*, 5, 749, doi: [10.1038/s41550-021-01398-w](https://doi.org/10.1038/s41550-021-01398-w)

- Ghirlanda, G., Salafia, O. S., Pescalli, A., et al. 2016, *A&A*, 594, A84, doi: [10.1051/0004-6361/201628993](https://doi.org/10.1051/0004-6361/201628993)
- Golomb, J., & Talbot, C. 2023, *Phys. Rev. D*, 108, 103009, doi: [10.1103/PhysRevD.108.103009](https://doi.org/10.1103/PhysRevD.108.103009)
- Hendriks, D. D., Van Son, L. A. C., Renzo, M., Izzard, R. G., & Farmer, R. 2023, *Monthly Notices of the Royal Astronomical Society*, stad2857, doi: [10.1093/mnras/stad2857](https://doi.org/10.1093/mnras/stad2857)
- Karathanasis, C., Mukherjee, S., & Mastrogiovanni, S. 2023, *Monthly Notices of the Royal Astronomical Society*, 523, 4539–4555, doi: [10.1093/mnras/stad1373](https://doi.org/10.1093/mnras/stad1373)
- Kimball, C., Talbot, C., Berry, C. P. L., et al. 2021, *ApJL*, 915, L35, doi: [10.3847/2041-8213/ac0aef](https://doi.org/10.3847/2041-8213/ac0aef)
- Kippenhahn, R., & Weigert, A. 1994, *Stellar structure and evolution*, 1st edn., *Astronomy and astrophysics library* (Berlin; New York: Springer-Verlag)
- Kovetz, E. D., Cholis, I., Breysse, P. C., & Kamionkowski, M. 2017, *PhRvD*, 95, 103010, doi: [10.1103/PhysRevD.95.103010](https://doi.org/10.1103/PhysRevD.95.103010)
- Kroupa, P. 2001, *Monthly Notices of the Royal Astronomical Society*, 322, 231–246, doi: [10.1046/j.1365-8711.2001.04022.x](https://doi.org/10.1046/j.1365-8711.2001.04022.x)
- Kroupa, P., & Jerabkova, T. 2019, *Nature Astronomy*, 3, 482–484, doi: [10.1038/s41550-019-0793-0](https://doi.org/10.1038/s41550-019-0793-0)
- Kunz, R., Fey, M., Jaeger, M., et al. 2002, *ApJ*, 567, 643, doi: [10.1086/338384](https://doi.org/10.1086/338384)
- LIGO Scientific Collaboration, & Virgo Collaboration. 2021, *ApJL*, 913, L7, doi: [10.3847/2041-8213/abe949](https://doi.org/10.3847/2041-8213/abe949)
- LIGO Scientific Collaboration, Virgo Collaboration, & KAGRA Collaboration. 2021, *GWTC-3: Compact Binary Coalescences Observed by LIGO and Virgo During the Second Part of the Third Observing Run — Parameter estimation data release*, Zenodo, doi: [10.5281/ZENODO.5546663](https://doi.org/10.5281/ZENODO.5546663)
- LIGO Scientific Collaboration, VIRGO Collaboration, & KAGRA Collaboration. 2023a, *Physical Review X*, 13, 011048, doi: [10.1103/PhysRevX.13.011048](https://doi.org/10.1103/PhysRevX.13.011048)
- LIGO Scientific Collaboration, VIRGO Collaboration, & Kagra Collaboration. 2023b, *ApJ*, 949, 76, doi: [10.3847/1538-4357/ac74bb](https://doi.org/10.3847/1538-4357/ac74bb)
- LIGO Scientific Collaboration, Virgo Collaboration, & KAGRA Collaboration. 2023c, *Physical Review X*, 13, doi: [10.1103/physrevx.13.011048](https://doi.org/10.1103/physrevx.13.011048)
- . 2023d, *GWTC-3: Compact Binary Coalescences Observed by LIGO and Virgo During the Second Part of the Third Observing Run — O3 search sensitivity estimates*, Zenodo, doi: [10.5281/ZENODO.7890437](https://doi.org/10.5281/ZENODO.7890437)
- Madau, P., & Dickinson, M. 2014, *Annual Review of Astronomy and Astrophysics*, 52, 415–486, doi: [10.1146/annurev-astro-081811-125615](https://doi.org/10.1146/annurev-astro-081811-125615)
- Maiolino, R., Nagao, T., Grazian, A., et al. 2008, *Astronomy & Astrophysics*, 488, 463
- Mancarella, M., Iacovelli, F., & Gerosa, D. 2023, *PhRvD*, 107, L101302, doi: [10.1103/PhysRevD.107.L101302](https://doi.org/10.1103/PhysRevD.107.L101302)
- Mandel, I., Farr, W. M., Colonna, A., et al. 2017, *MNRAS*, 465, 3254, doi: [10.1093/mnras/stw2883](https://doi.org/10.1093/mnras/stw2883)
- Mandel, I., Farr, W. M., & Gair, J. R. 2019, *MNRAS*, 486, 1086, doi: [10.1093/mnras/stz896](https://doi.org/10.1093/mnras/stz896)
- Marchant, P., Renzo, M., Farmer, R., et al. 2019, *The Astrophysical Journal*, 882, 36, doi: [10.3847/1538-4357/ab3426](https://doi.org/10.3847/1538-4357/ab3426)
- Mehta, A. K., Buonanno, A., Gair, J., et al. 2022, *The Astrophysical Journal*, 924, 39, doi: [10.3847/1538-4357/ac3130](https://doi.org/10.3847/1538-4357/ac3130)
- Miller, M. C., & Hamilton, D. P. 2002, *ApJ*, 576, 894, doi: [10.1086/341788](https://doi.org/10.1086/341788)
- Ng, K. K. Y., Vitale, S., Farr, W. M., & Rodriguez, C. L. 2021, *ApJL*, 913, L5, doi: [10.3847/2041-8213/abf8be](https://doi.org/10.3847/2041-8213/abf8be)
- Paxton, B., Smolec, R., Schwab, J., et al. 2019, *ApJS*, 243, 10, doi: [10.3847/1538-4365/ab2241](https://doi.org/10.3847/1538-4365/ab2241)
- Payne, E., Isi, M., Chatziioannou, K., & Farr, W. M. 2023. <https://arxiv.org/abs/2309.04528>
- Phan, D., Pradhan, N., & Jankowiak, M. 2019, *arXiv preprint arXiv:1912.11554*
- Planck Collaboration. 2020, *A&A*, 641, A6, doi: [10.1051/0004-6361/201833910](https://doi.org/10.1051/0004-6361/201833910)
- Rahman, N., Janka, H.-T., Stockinger, G., & Woosley, S. E. 2022, *Monthly Notices of the Royal Astronomical Society*, 512, 4503–4540, doi: [10.1093/mnras/stac758](https://doi.org/10.1093/mnras/stac758)
- Rakavy, G., & Shaviv, G. 1967, *ApJ*, 148, 803, doi: [10.1086/149204](https://doi.org/10.1086/149204)
- Ray, A., Magaña Hernandez, I., Mohite, S., Creighton, J., & Kapadia, S. 2023, *arXiv e-prints*, arXiv:2304.08046, doi: [10.48550/arXiv.2304.08046](https://doi.org/10.48550/arXiv.2304.08046)
- Rodriguez, C. L., Zevin, M., Amaro-Seoane, P., et al. 2019, *PhRvD*, 100, 043027, doi: [10.1103/PhysRevD.100.043027](https://doi.org/10.1103/PhysRevD.100.043027)
- Safarzadeh, M., & Farr, W. M. 2019, *The Astrophysical Journal*, 883, L24, doi: [10.3847/2041-8213/ab40bd](https://doi.org/10.3847/2041-8213/ab40bd)
- Sallaska, A. L., Iliadis, C., Champagne, A. E., et al. 2013, *ApJS*, 207, 18, doi: [10.1088/0067-0049/207/1/18](https://doi.org/10.1088/0067-0049/207/1/18)
- Salpeter, E. E. 1955, *ApJ*, 121, 161, doi: [10.1086/145971](https://doi.org/10.1086/145971)
- Schneider, F. R. N., Sana, H., Evans, C. J., et al. 2018, *Science*, 359, 69, doi: [10.1126/science.aan0106](https://doi.org/10.1126/science.aan0106)
- Stevenson, S., Sampson, M., Powell, J., et al. 2019, *ApJ*, 882, 121, doi: [10.3847/1538-4357/ab3981](https://doi.org/10.3847/1538-4357/ab3981)
- Talbot, C., Smith, R., Thrane, E., & Poole, G. B. 2019, *PhRvD*, 100, 043030, doi: [10.1103/PhysRevD.100.043030](https://doi.org/10.1103/PhysRevD.100.043030)
- Talbot, C., & Thrane, E. 2017, *Phys. Rev. D*, 96, 023012, doi: [10.1103/PhysRevD.96.023012](https://doi.org/10.1103/PhysRevD.96.023012)

- Talbot, C., & Thrane, E. 2018, *ApJ*, 856, 173,
doi: [10.3847/1538-4357/aab34c](https://doi.org/10.3847/1538-4357/aab34c)
- Thrane, E., & Talbot, C. 2019, *PASA*, 36, e010,
doi: [10.1017/pasa.2019.2](https://doi.org/10.1017/pasa.2019.2)
- Tiwari, V. 2018, *Classical and Quantum Gravity*, 35,
145009, doi: [10.1088/1361-6382/aac89d](https://doi.org/10.1088/1361-6382/aac89d)
- Tiwari, V., & Fairhurst, S. 2021, *ApJL*, 913, L19,
doi: [10.3847/2041-8213/abfbc7](https://doi.org/10.3847/2041-8213/abfbc7)
- Van Son, L. A. C., De Mink, S. E., Callister, T., et al. 2022,
The Astrophysical Journal, 931, 17,
doi: [10.3847/1538-4357/ac64a3](https://doi.org/10.3847/1538-4357/ac64a3)
- Vangioni, E., Olive, K. A., Prestegard, T., et al. 2015,
MNRAS, 447, 2575, doi: [10.1093/mnras/stu2600](https://doi.org/10.1093/mnras/stu2600)
- Vitale, S., Farr, W. M., Ng, K. K. Y., & Rodriguez, C. L.
2019, *ApJL*, 886, L1, doi: [10.3847/2041-8213/ab50c0](https://doi.org/10.3847/2041-8213/ab50c0)
- Wong, K. W. K., Breivik, K., Farr, W. M., & Luger, R.
2023, *ApJ*, 950, 181, doi: [10.3847/1538-4357/acc863](https://doi.org/10.3847/1538-4357/acc863)
- Woosley, S. E. 2017, *ApJ*, 836, 244,
doi: [10.3847/1538-4357/836/2/244](https://doi.org/10.3847/1538-4357/836/2/244)
- Woosley, S. E. 2019, *The Astrophysical Journal*, 878, 49,
doi: [10.3847/1538-4357/ab1b41](https://doi.org/10.3847/1538-4357/ab1b41)
- Woosley, S. E., & Heger, A. 2021, *The Astrophysical
Journal Letters*, 912, L31, doi: [10.3847/2041-8213/abf2c4](https://doi.org/10.3847/2041-8213/abf2c4)
- Zevin, M., Pankow, C., Rodriguez, C. L., et al. 2017, *ApJ*,
846, 82, doi: [10.3847/1538-4357/aa8408](https://doi.org/10.3847/1538-4357/aa8408)